Computational and Structural Biotechnology Journal 18 (2020) 2357–2372

COMPUTATIONAL AND STRUCTURAL BIOTECHNOLOGY JOURNAL

journal homepage: www.elsevier.com/locate/csbj

Conformational ensembles of non-peptide ω-conotoxin mimetics and Ca^{+2} ion binding to human voltage-gated N-type calcium channel $Ca_v2.2$

Sameera [a], Fawad Ali Shah [b], Sajid Rashid [a,*]

[a] National Center for Bioinformatics, Quaid-i-Azam University, Islamabad, Pakistan
[b] Riphah Institute of Pharmaceutical Sciences, Riphah International University, Islamabad, Pakistan

ARTICLE INFO

Article history:
Received 29 May 2020
Received in revised form 24 August 2020
Accepted 26 August 2020
Available online 3 September 2020

Keywords:
Chronic neuropathic pain
N-type voltage-gated calcium channel ($Ca_v2.2$)
Non-peptide ω-conotoxin mimetics inhibitor
Synaptic transmission

ABSTRACT

Chronic neuropathic pain is the most complex and challenging clinical problem of a population that sets a major physical and economic burden at the global level. Ca^{2+}-permeable channels functionally orchestrate the processing of pain signals. Among them, N-type voltage-gated calcium channels (VGCC) hold prominent contribution in the pain signal transduction and serve as prime targets for synaptic transmission block and attenuation of neuropathic pain. Here, we present detailed *in silico* analysis to comprehend the underlying conformational changes upon Ca^{2+} ion passage through $Ca_v2.2$ to differentially correlate subtle transitions induced via binding of a conopeptide-mimetic alkylphenyl ether-based analogue MVIIA. Interestingly, pronounced conformational changes were witnessed at the proximal carboxyl-terminus of $Ca_v2.2$ that attained an upright orientation upon Ca^{+2} ion permeability. Moreover, remarkable changes were observed in the architecture of channel tunnel. These findings illustrate that inhibitor binding to $Ca_v2.2$ may induce more narrowing in the pore size as compared to Ca^{2+} binding through modulating the hydrophilicity pattern at the selectivity region. A significant reduction in the tunnel volume at the selectivity filter and its enhancement at the activation gate of Ca^{+2}-bound $Ca_v2.2$ suggests that ion binding modulates the outward splaying of pore-lining S6 helices to open the voltage gate. Overall, current study delineates dynamic conformational ensembles in terms of Ca^{+2} ion and MVIIA-associated structural implications in the $Ca_v2.2$ that may help in better therapeutic intervention to chronic and neuropathic pain management.

1. Introduction

Chronic pain is a serious health issue that affects more than 25% of the world's population, and is increasing with the population ages [1]. Approximately, 8% of general population is affected by neuropathic pain [2] that is abnormal signaling due to injury or malfunction in the peripheral or central nervous system resulting in exaggerated pain sensations [3–6]. It originates from plastic changes at peripheral, spinal, or supraspinal sites known as peripheral neuropathies (postherpetic neuralgia, toxic neuropathies and focal traumatic neuropathies), central neuropathies (ischemic cerebrovascular injury, spinal cord injury and Parkinson's disease) and mixed neuropathies (diabetic neuropathies, sympathetically maintained pain) [4]. Neuropathic pain has challenged the biomedical research to develop more effective drugs. Many drugs that treat inflammatory pain, such as Nonsteroidal anti-inflammatory drugs (NSAIDs) or opioids are in general much less effective in relieving neuropathic pain and exhibit efficacy only at high doses or when administered by more invasive (e.g., intraspinal) routes. Currently, neuropathic pain is treated mostly by tricyclic antidepressants, specific serotonin and norepinephrine modulators, and sodium and calcium channel modulators [7]. Currently, only 3 Food and Drug Administration (FDA) approved drugs, gabapentin, pregabalin and ziconotide target voltage-gated calcium channels (VGCCs); however, pregabalin and gabapentin have serious side effects and low efficacy issues [8]. The ω-conotoxin MVIIA or Ziconotide (SNX-11; Prialt®) is a novel non-opioid analgesic drug that is a synthetic version from a large class of marine cone snail peptides [9–11]. This drug has been approved for the symptomatic management of severe chronic pain. It is administered intrathecally to attain optimal analgesic efficacy along with less serious side-effects as it has limited ability to cross blood–brain barrier [11]. This has prompted the development of dozens of small-molecule blockers that are effective in the animal models [12–13].

* Corresponding author.
E-mail address: sajidrwp@yahoo.co.uk (S. Rashid).

https://doi.org/10.1016/j.csbj.2020.08.027

Animal studies demonstrate that due to peripheral tissue inflammation or nerve injury, $Ca_v2.2$ (N-type Ca^{2+} channel subunit alpha-1B) expression is enhanced in the dorsal horn [14–15]. $Ca_v2.2$ deficient mice exhibit hyposensitivity to inflammatory and neuropathic pain [16–18]. Hence, this channel is considered as an important target for treating nociceptive and neuropathic pain [19–22]. $Ca_v2.2$ is a transmembrane VGCC that is involved in various cell signaling responses and membrane potential alterations that induce calcium influx. As a result, intracellular calcium level elevates to micro molar range [23] that stimulates various calcium channel processes, i.e., gene transcription, membrane excitability, neurotransmitter release, neurite outgrowth and activation of calcium-dependent enzymes such as calmodulin-dependent protein kinase II (CaMKII) and protein kinase C (PKC) [24]. The prolonged elevation of intracellular calcium levels is cytotoxic [25] as the intrinsic gating processes and cell signaling pathways tightly regulate the channel activity and trafficking to and from membrane [26]. The blockage of synaptic transmission through $Ca_v2.2$ serves as a prime mechanism for the reduction of pain signals to the central nervous system [27]. $Ca_v2.2$ is a complex ion channel protein that is comprised of 4 or 5 different subunits encoded by multiple genes. The largest and most important subunit is α1 subunit of 262 kDa molecular weight that is encoded by *CACNA1B* gene in human [28]. All $Ca_v\alpha1$ subunits of VGCC possess a common transmembrane topology in all transmembrane domains. Their important functions include pore conduction, voltage sensing, gating apparatus and channel regulation [29]. $Ca_v\alpha1$ subunits have four homologous domains (D_I-D_{IV}), each having six transmembrane segments (S1-S6). S4 helix is voltage-sensing segment, while the loop between S5 and S6 segments in each domain is involved in pore formation [29]. It involves in ion conductance and selectivity. In addition to α1-subunit, VGCCs are composed of other subunits that are β-subunits, α2δ-subunits and γ-subunits. Among them, 4 β- and α2δ-subunits, while 8 γ-subunits are involved in enhancing α1-subunit cell surface expression and its interaction with diverse intracellular signaling molecules that modulate the gating properties [30–32].

Animal venoms have high efficacy and selectivity against a wide range of biological targets such as membrane proteins i.e., ion channels, receptors and transporters [33–36]. To date, about 500–700 *Conus* species have been identified [37] containing valuable neuroactive peptides. Multiple attempts have been made to develop conopeptide mimetics and small molecule inhibitors against VGCCs. Among 21 ω-conotoxin peptides identified so far [38–39], the most well characterized ω-conotoxins are $Ca_v2.2$ blockers: MVIIA, CVID and GVIA [40]. Here we characterized the published conopeptide-mimetic inhibitors that are based on diverse scaffolds i.e., dendritic scaffold [41], benzothiazole derivative [42], anthranilamide derivative [43], anthranilamide scaffold [44] and anthranilamide compounds with diphenylmethylpiperazine moiety [40] to block $Ca_v2.2$ (Table S1). Our *in-silico* analysis provides significant information about the binding pattern and its impact on the $Ca_v2.2$ channel conformation and activity. By exploring the association of $Ca_v2.2$ and small-molecule conopeptide-mimetic inhibitors, our study may provide invaluable insights into the potential anesthetic and analgesic impact on pain by multi-targeted inhibition.

2. Methodology

2.1. Molecular modeling of Cav2.2

The amino acid sequence of *Homo sapiens* α1-subunit of $Ca_v2.2$ was retrieved through UniProtKB (*www.uniprot.org*) having an accession number: Q00975. Due to lack of crystal structure, *Oryctolagus cuniculus* voltage-gated calcium channel, $Ca_v1.1$ (PDB ID: 5GJW; resolution: 3.6 Å; sequence coverage: 63% (70-1873AA); sequence identity: 50%;) structure [45] was used as a template to model α1-subunit of *Homo sapiens* $Ca_v2.2$ through SWISS-MODEL (*swissmodel.expasy.org*). The modeled structure of Human $Ca_v2.2$ (contains 1771 residues (Phe76-Pro1846)) exhibits 0.45 global quality estimation score (GMQE) and 44% sequence similarity. The predicted structure was visualized by UCSF Chimera 1.11.2 [46]. The poor rotamers and outliers in predicted model was refined by WinCoot [47] and subsequently validated by multiple evaluation tools. MolProbity server (*http://molprobity.manchester.ac.uk/*) was used to analyze the Ramachandran score, Ramachandran outliers, poor and favored rotamers, bad angles and bonds. ERRAT server (*https://servicesn.mbi.ucla.edu/ERRAT/*) was utilized to calculate the overall quality factor of modeled structure.

2.2. Selection of inhibitors

Initially, 30 inhibitors were retrieved against $Ca_v2.2$ through extensive literature survey (Table S1). These inhibitors were non-peptide mimetics of ω-conotoxins (MVIIA, CVID and GVIA) isolated from cone snail. From these 30 inhibitors, 7 compounds were filtered out based on their pore binding positions (Table S2). In C1, three important amino acids mimetics (R10, L11 and Y13) of ω-conotoxin MVIIA were attached to dendritic scaffold [41]. In C2-4 benzothiazole scaffold [48,38] and in C5 and C6 contained anthranilamide scaffold that projected the side chain mimetics of the key residues (K2, Y13 and R17) in ω-conotoxin GVIA [43,48]. C7 shared a similar pattern to that of C6, except bearing an anthranilamide scaffold that was modified by replacing phenoxyaniline substituent with a diphenylmethylpiperazine moiety [40]. 2D structures of these inhibitors were drawn by ChemDraw Pro 12.0 [49] and converted into 3D coordinates that were further energy minimized using Avogadro® [50] tool through Merck Molecular Force Field (MMFF94) and steepest descent algorithm [51].

2.3. Molecular docking analysis

Molecular docking analysis was performed through PatchDock [52] to evaluate the interaction pattern of $Ca_v2.2$ with Ca^{2+} ion and selected compounds. For $Ca_v2.2$ and Ca^{2+} ion docking, Ca^{2+} ion selective and permeable residues of $Ca_v2.2$ were obtained through UniProtKB (*www.uniprot.org/uniprot/Q00975*), were provided. For all docking runs, modeled $Ca_v2.2$ and compounds were subjected to rigid docking though small-scale flexibility, implicitly by allowing few steric clashes and intermolecular penetrations. PatchDock identifies geometric patches through segmentation algorithm, surface matching, filtering and scoring [52]. After detailed comparative analysis of the binding sites of inhibitors, suitable candidate solutions were chosen on the basis of Root Mean Square Deviation (RMSD) clustering. Based on these findings, out of 30 docked compounds (Table S1, Fig. S1) only 7 were shortlisted on the basis of their binding abilities at the ion selectivity and permeability region of $Ca_v2.2$ pore (Table S2). These compounds were further scrutinized by published IC_{50} values [40–44]. The interactions were carefully evaluated through UCSF Chimera 1.11.2 [46]. Graphical visualization of hydrogen bonding, hydrophobic and electrostatic interactions were analyzed by LigPlus [53] and Discovery Studio 4.5 [54].

2.4. Molecular dynamics simulation analysis

C1 was selected for detailed analysis owing to its binding preference at the SF ring of pore region by interacting with three residues of EEEE motif (E314, E663, and E1365) (Table S2). In order to

evaluate comparative conformational readjustments, apo-$Ca_v2.2$, Ca^{2+} ion and C1-bound modeled $Ca_v2.2$ (1771 residues; Phe76-Pro1846) complexes were subjected to MD simulation assay through Visual Molecular Dynamics (VMD) [55] and Nanoscale Molecular Dynamics (NAMD) tools [56]. For all three systems, *psfgen* plugin of VMD was utilized to generate protein structure files (PSF). These structures were solvated by Heimut Grubmuller's SOLVATE program [57] that fills empty space inside the pores by surrounding it with water. The undesired water molecules were removed. The solvated structures were embedded in the remaining system by deleting unwanted water molecules in the hydrophobic region of $Ca_v2.2$ using VMD.

An automated system of VMD generated lipid bilayer by *Membrane Builder* by specifying 1-palmityol 2-oleoyl phosphatidylcholine (POPC) membrane patch of length 128 Å in X and Y coordinates and CHARMM27 force field [58]. VMD was utilized to align partially solvated $Ca_v2.2$ tetramer with POPC lipid membrane. $Ca_v2.2$ was settled in the membrane with the hydrophobic residues; while, the orientation of protein was adjusted to avoid its overlap with lipid molecules. Subsequently, the overlapping water molecules were removed. VMD *Solvate* plugin was used for the solvation of entire system by placing it in the specified size water box. Ionization of all systems was performed by VMD *Autoionize* plugin that generates specific ionic concentration of NaCl (0.4 mmol/L) and transmutes water molecules into ions. The membrane patches were initially equilibrated by short simulation runs (0.5 ns) while keeping the system static, except lipid tails to disorder in fluid-like bilayer. The temperature was set to 300 K by employing Langevin dynamics to maintain constant temperature and 1 atm pressure (by Langevin piston method) throughout production simulation. Minimizations were carried out for 1000 steps. NAMD 2.9 was used to perform the equilibrium MD simulations for all systems. Instead of standard CHARMM parameter file, a modified parameter file containing "NBFIX" with correction for carbonyl oxygen-Ca^{2+} ion interaction (distance restrained to 2.85 Å) was used. This correction is essential for the selectivity filter (SF) in $Ca_v2.2$. SwissParam [59] was utilized for the topology file generation of compounds. The periodic boundary conditions (PBC) and Particle Mesh Ewald (PME) grid size was also set for all systems in the NAMD configuration files. The outputs were analyzed having disordered lipid tails. MD simulations were run with full dynamics that are essential for the setting of unusual atomic positions in the systems, followed by minimization and equilibration. Harmonic constraints were enforced on $Ca_v2.2$. The minimization and equilibration steps were executed for 0.5 ns by NAMD2 [56]. The full systems were then equilibrated by keeping protein channel unconstrained for 0.5 ns. Fully equilibrated systems were analyzed by computing Root Mean Square Deviation (RMSD) and Root mean square fluctuation (RMSF) plots through VMD. The final production runs were carried out for 100 ns. The resulting outputs were analyzed by VMD tool [55] and UCSF Chimera 1.11.2 [46].

3. Results

3.1. Model analysis of $Ca_v2.2$

The crystal structure of *Oryctolagus cuniculus* $Ca_v1.1$ [60] (PDB ID: 5GJW; resolution: 3.6 Å; sequence coverage: 63%; sequence identity: 50%) was selected as a template to model 3D structure of $Ca_v2.2$ through SWISS-MODEL (*swissmodel.expasy.org*). An RMSD value of 0.196 Å was observed upon superimposition of template and target structures. Ramachandran plot designated the presence of 90.23% residues of $Ca_v2.2$-modeled structure in the favored region, 97.60% residues as favored rotamers, 0.17% residues as poor rotamers and 1.46% residues as Ramachandran outliers. The observed ERRAT quality factor value was 81.46%.

Human $Ca_v2.2$ also known as N-type calcium channel consists of 2,339 residues with a molecular mass of ~262 kDa comprises 4 domains (D_I-D_{IV}), each contains 6 transmembrane (S1-S6) α-helices (Fig. 1A) [45]. Two helices (S5 and S6) from each domain constitute a pore that is essential for the conduction of Ca^{2+} ions (Fig. 1) [45]. The voltage sensor domain (VSD) consists of 4 helices (S1-S4) in each domain (Movie S1). Any voltage change across the cell membrane is sensed by VSD that surrounds the pore region. In between the S5 and S6 helices, a P-loop is present that acts as a selectivity filter for Ca^{2+} ion permeability [45]. The N- and C-termini of channel are localized in the cytoplasmic environment. In addition to these four domains, there are two additional domains named as EF-hand (helix-loop-helix domain) and IQ (isoleucine-glutamine motif) that are crucial for Ca^{2+} binding. EF-hand is a helical domain that is flanked by a 12-residue loop from both sides [61]. It is involved in binding with Ca^{2+} ions through undergoing multiple conformational changes [61]. IQ motif in IQ domain interacts with Ca^{2+}/calmodulin.

3.2. Ca^{2+} ion coordination

As voltage-gated calcium channels (VGCCs) allow Ca^{2+} ions to pass through the pore region, Ca^{2+} ions were coordinated with the modeled $Ca_v2.2$ structure. Among surrounding residues, Glu314 and Glu1365 residues potentially coordinated with Ca^{2+} ion having bond lengths of 3.12 Å and 3.25 Å, respectively (Fig. 2).

3.3. Molecular docking analysis

Multiple reports suggested that non-peptide analogues of ω-conotoxins may target $Ca_v2.2$ channels [38,41,43,70,83–85]. These non-peptide conotoxin mimetics mimic the scaffolds of ω-conotoxin MVIIA, CVID and GVIA [62]. In total, out of 30 docked compounds (Fig. S1; Table S1), 7 [40–44] were selected on the basis of their binding pattern at the pore region of $Ca_v2.2$ shared by S5 and S6 helices along with P-loop of each domain (Fig. 4, S2). These compounds contain dendritic, benzothiazole or anthranilamide scaffolds, attached with Y, L/K and R residues (Fig. 3, Table S2). The IC_{50} values of 7 selected compounds against $Ca_v2.2$ are listed in Table S2. Compound C1 exhibits a dendritic scaffold. C2-4 contain benzothiazole, C5-6 have anthranilamide scaffold, whereas C7 holds a modified anthranilamide scaffold with a phenoxyaniline group that is replaced into diphenylmethylpiperazine moiety. These compounds may be used for the treatment of chronic and neuropathic pain by blocking $Ca_v2.2$ VGCCs.

Compound C1 interacted with the residues of pore and S6 segments of $Ca_v2.2$. It exhibited favorable associations with 3 of the selectivity filter (SF) ring residues (Glu314, Glu663 and Glu1365) (Fig. 4I). Compounds C2 and C3 binding was prompted through hydrophobic association with residues of D_I (pore), D_{III} (S5, pore and S6) and D_{IV} (pore and S6). Ala1652, Thr1653, Ser1696 residues of $Ca_v2.2$ were involved in hydrogen bonding with both compounds (Fig. 4II, 4III). C4 exhibited association with D_{III} (S5, pore and S6) and D_{IV} (pore and S6), while a single hydrogen bond was observed with O-atom of Thr1653 residue (Fig. 4IV). Contrary to C2-C4, compounds C5-C6 showed interactions with the residues of D_I (S5, pore and S6) and D_{II} (S6). Moreover, a single H-bond was observed via Asn697 and Met313 residues, respectively (Fig. 4V, 4VI). Compound C7 exhibited a favorable number of hydrophobic associations with the residues of D_I (S5, pore and S6), D_{II} (S6), D_{III} (pore) and D_{IV} (pore). Furthermore, Met347, Asn697, Thr1653 and Thr1363 residues exhibited hydrogen bonding (Fig. 4VII). The schematic binding details are indicated in Fig. S2. These findings illustrate that only compound C1 exhibited

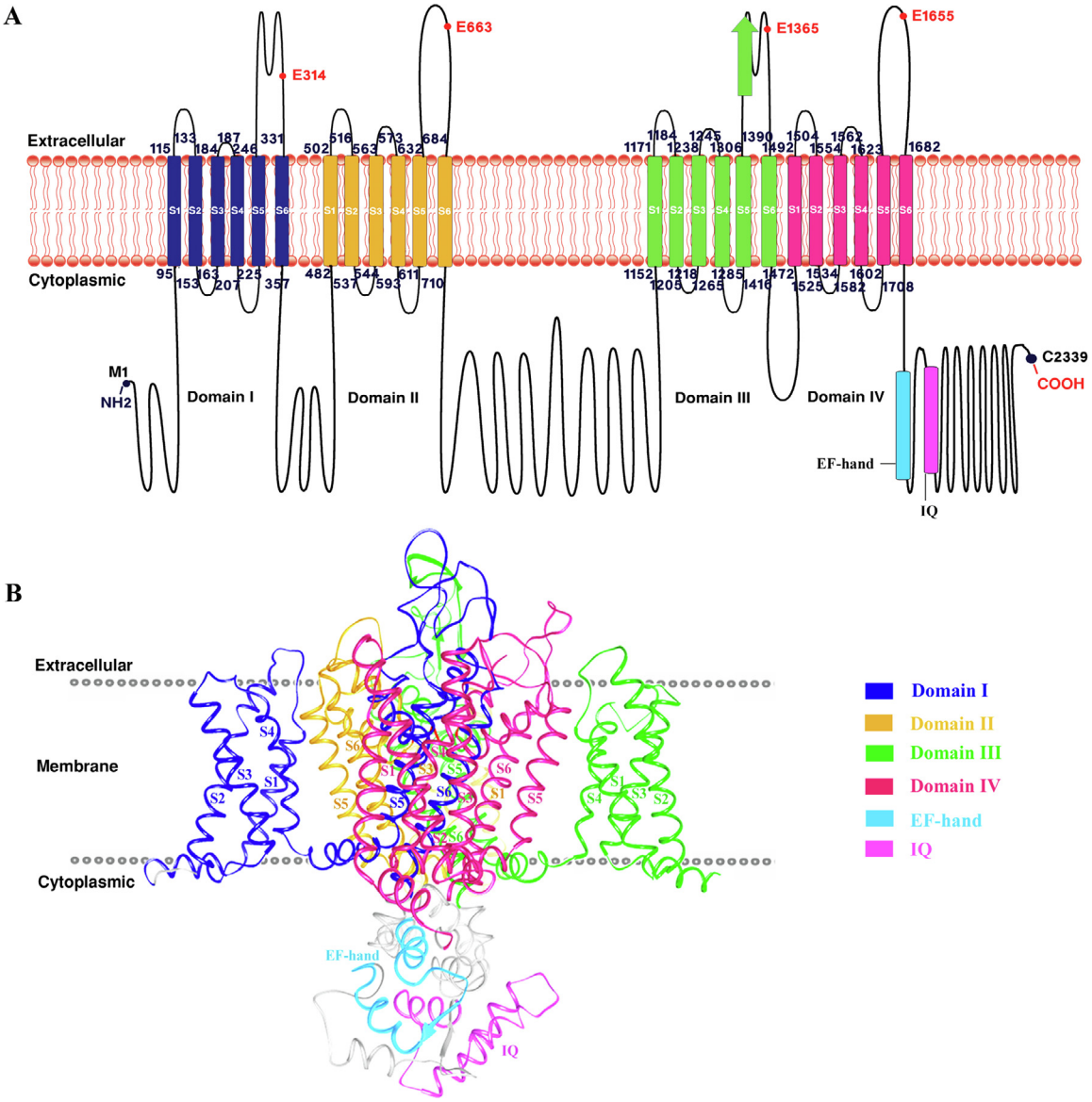

Fig. 1. N-type Ca^{2+} channel subunit alpha-1B (Cav2.2) structural and topological representation. (A) $Ca_v2.2$ specific domains DI-DIV, represented by corresponding colors. Each domain consists of six transmembrane segments (S1-S6), connected by P-loops. The starting and ending residues of segments are labeled in dark blue color along with the glutamate residue in P-loop between S5 and S6 that is important for Ca^{2+} ion permeability and selectivity (shown in red color). The EF-hand domain is indicated in sky blue color, while IQ domain is shown in orchid color. (B) Homology model of $Ca_v2.2$ indicating the membrane organization and helical arrangement in the respective color. The loop regions between the domains of modeled structure is hidden to avoid ambiguity. (For interpretation of the references to color in this figure legend, the reader is referred to the web version of this article.)

bonding with three residues (E314, E663, and E1365) of the Ca^{2+} ion SF ring, therefore, compound C1 may be a good choice for MD simulation assay.

3.4. Molecular dynamics simulation analysis

Compound C1 was selected for detailed binding pattern and conformational ensemble study based on its localization at the SF ring and central cavity of pore. In order to explore the overall stability and time-dependent conformational transitions in $Ca_v2.2$ upon binding to C1 and Ca^{+2} ions, molecular dynamics (MD) simulations were performed by utilizing Visual Molecular Dynamics (VMD) and Nanoscale Molecular Dynamics (NAMD) tools. Systems preparation (apo-$Ca_v2.2$, $Ca_v2.2$-Ca^{2+} ion and $Ca_v2.2$-C1) for MD simulations were carried out by wrapping the $Ca_v2.2$ structural model in 1-palmityol 2-oleoyl phosphatidylcholine (POPC) membrane to create a native-like surrounding (Fig. S5). All systems were minimized and equilibrated to analyze the passage of Ca^{2+} ions through embedded ion channel in the lipid membrane.

The overall protein stability and time-dependent interactions were monitored by generating PDB files at different time intervals. Subsequently, underlying conformational and structural changes in the protein channel in association with Ca^{2+} ion and C1 were analyzed. Root mean square deviation (RMSD), root mean square fluctuation (RMSF), radius of gyration (Rg), radial pair distribution function g(r) and number of hydrogen bonds were calculated throughout 100 ns time scale.

To examine the convergence in all three systems, RMSD values computed through Cα-atoms were plotted against time (Fig. 5A). RMSD scores observed over 100 ns for apo-$Ca_v2.2$ and both complexes displayed an abrupt rise up to 10 nm. All simulated structures acquired a stable state at 40 ns. The apo-$Ca_v2.2$ and Ca^{2+}-

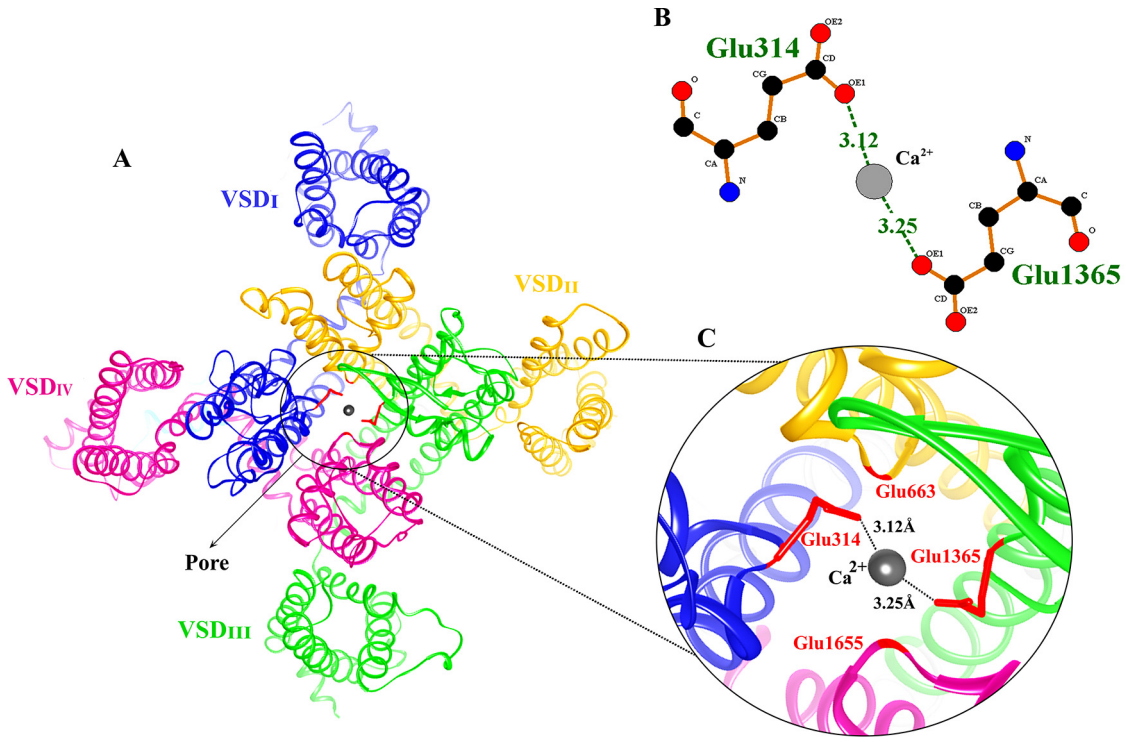

Fig. 2. Ca^{2+} ion coordination at the selectivity filter (SF) ring of $Ca_v2.2$. (A) Top view of $Ca_v2.2$. The four homologous repeats exhibit a clockwise arrangement, when viewed from extracellular side. VSD of each domain is labeled by specific colors. Glu residues responsible for the Ca^{2+} ion selectivity and permeability are shown in red sticks. (B) Interactions are analyzed by LigPlus [53]. (C) The positions of Glu residues are labeled in respective colors. The distances between them are illustrated by dotted lines. (For interpretation of the references to color in this figure legend, the reader is referred to the web version of this article.)

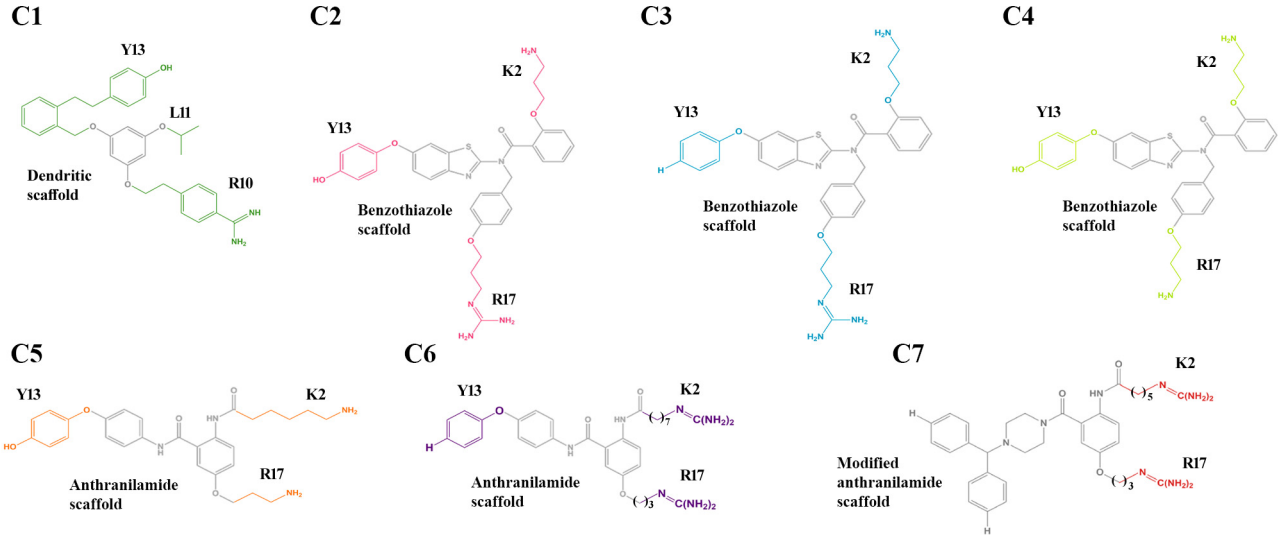

Fig. 3. 2D structures of selected mimetics. C1, MVIIA (dendritic scaffold attached to Y13, L11 and R10 residues); C2, CVID (benzothiazole scaffold attached to K2, Y13 and R17 residues); C3, GVIA (benzothiazole scaffold attach to K2, Y13 and R17 residues); C4, GVIA (benzothiazole scaffold attached to K2, Y13 and R17 residues); C5, GVIA (anthranilamide scaffold attached to K2, Y13 and R17 residues); C6, GVIA (anthranilamide scaffold attached to K2, Y13 and R17 residues) and C7, GVIA (modified anthranilamide scaffold attached to K2 and R17 residues) [41,48,38,43,40]. The scaffolds are indicated in grey color.

bound $Ca_v2.2$ attained a stable state within a range of 11–15 nm whereas, C1-bound $Ca_v2.2$ demonstrated an increasing trend in the RMSD profile (18–19 nm). RMSF plot revealed certain fluctuating residues at the loop regions of $Ca_v2.2$ between D_{II} and D_{III} (Fig. 5B, Table 1). Glu314, Glu663, Glu1365 and Glu1655 residues of SF ring involved in Ca^{2+} ion selective permeability exhibited lower fluctuations during simulation assays; however, these residues were more stable in $Ca_v2.2$-Ca^{2+} complex as compared to apo-$Ca_v2.2$ and $Ca_v2.2$-C1 complex. In addition to SF ring, Gly353, Ala706, Ala1413 and Ala1705 residues (the G/A/A/A ring) at inner gate of channel and interacting residues lying at S4-S5 linker were quite stable in both complexes. Major fluctuations were observed in the loop regions, while α-helices and ion selectivity residues remained stable during the course of simulation.

Radius of gyration (Rg) values were calculated for both complexes and apo-$Ca_v2.2$ to get insight into compactness of protein

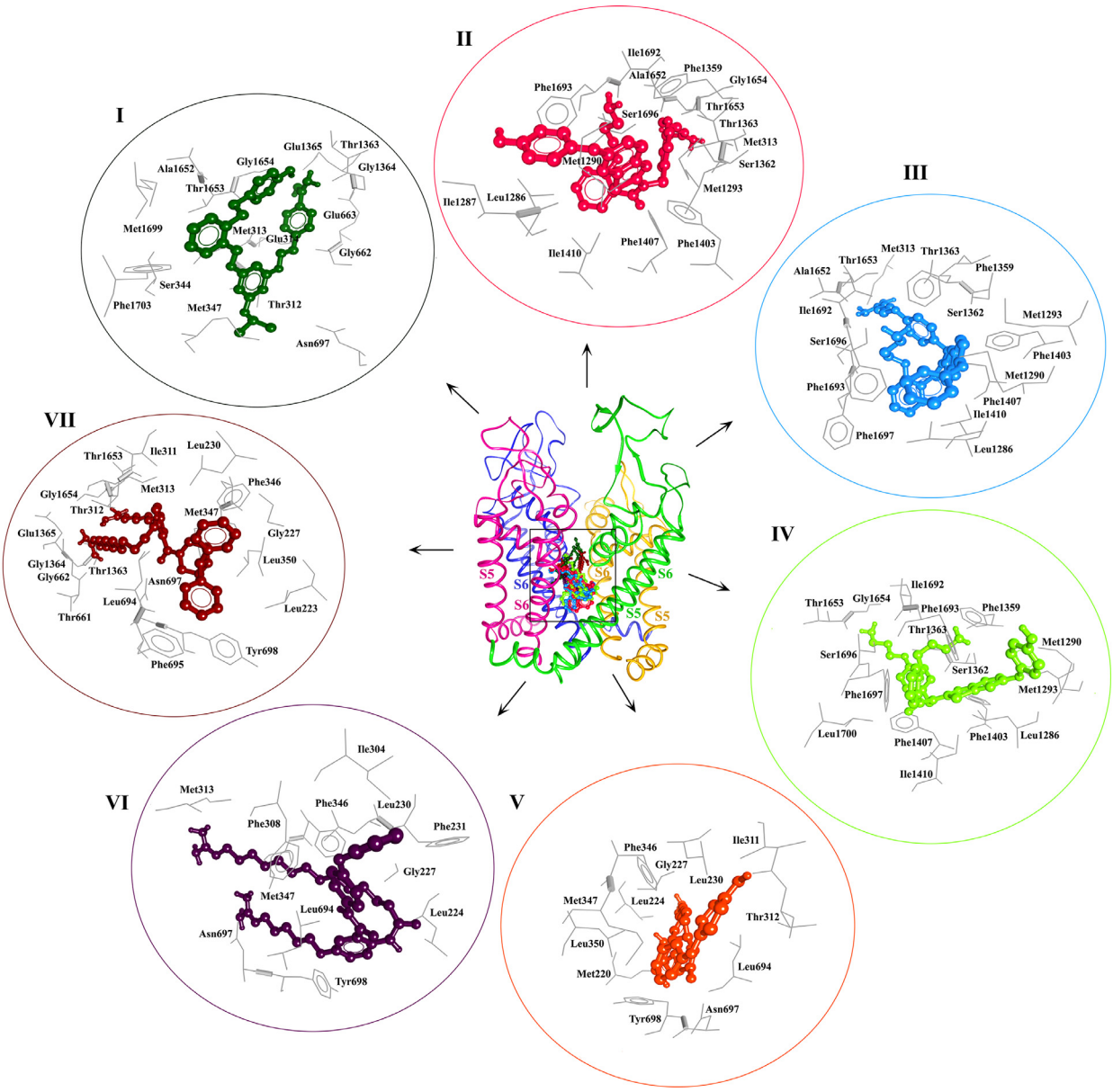

Fig. 4. Binding analysis of compounds C1-7 and $Ca_v2.2$. C1-7 are shown in dark green, dark pink, dark sky blue, chartreuse, orange, dark magenta and firebrick colors in circles I-VII, respectively. The channel interacting residues are shown in grey wires and labeled in black color. (For interpretation of the references to color in this figure legend, the reader is referred to the web version of this article.)

throughout MD simulation. Rg analysis provides quantitative information about changes in the tertiary structures linked to the compactness of the simulated system. Higher Rg values from the original depict the protein structure expansion. The apo-$Ca_v2.2$ exhibited a decreasing trend in Rg values from 56.74 Å to 52.5 Å, highlighting the compactness of system at 40 ns onwards. The structural equilibrium for Ca^{2+}-bound $Ca_v2.2$ was observed throughout the simulation assay with the Rg values ranging between 55.79 Å and 57.17 Å, indicating the consistent system compactness (Fig. 5C). The highest values of Rg for C1-bound $Ca_v2.2$ complex was detected as 58.96 Å during 1 ns of MD simulation. Afterward, Rg values gradually decreased up to 52 Å at 70 ns of time scale and remained stable up to 100 ns. Consequently, $Ca_v2.2$-C1 complex exhibited a tight packing as compared to Ca^{+2}-bound $Ca_v2.2$ suggesting more firmness in channel upon binding to C1. MD simulation trajectory files for both complexes were analyzed for hydrogen bond interactions, which remained stable during the entire simulation time (Fig. 5D). The highest numbers of hydrogen bonds in Ca^{2+}-bound and C1-bound $Ca_v2.2$ were observed at 45.8 ns (403) and 89.4 ns (417), respectively.

Radial pair distribution function g(r) provides the probability of finding particles at a certain distance r. G(r) values were calculated for four residues (Glu314, Glu663, Glu1365 and Glu1655) that form SF ring to explore their distances with Ca^{2+} ion (Fig. 6A,B). The atom OE1 of Glu314 exhibited interactions with Ca^{2+} ion. OE1 atoms of Glu314 and Glu1365 residues more likely preferred to localize (11832.6 and 10041.5 times) in the vicinity of Ca^{2+} ion at a distance of 2.15 Å (Table 2). Similarly, OE1 atoms of Glu663 and Glu1655 residues exhibited highest peaks at distances of 2.25 Å and 4.85 Å, respectively. Interatomic distance calculation among Glu314, Glu663, Glu1365 and Glu1655 residues suggested that Glu1365-Glu1655 residues were closer to Ca^{+2} ion at a distance of 3.75 Å whereas, Glu663-Glu1655 residues exhibited a distance of 8.65 Å.

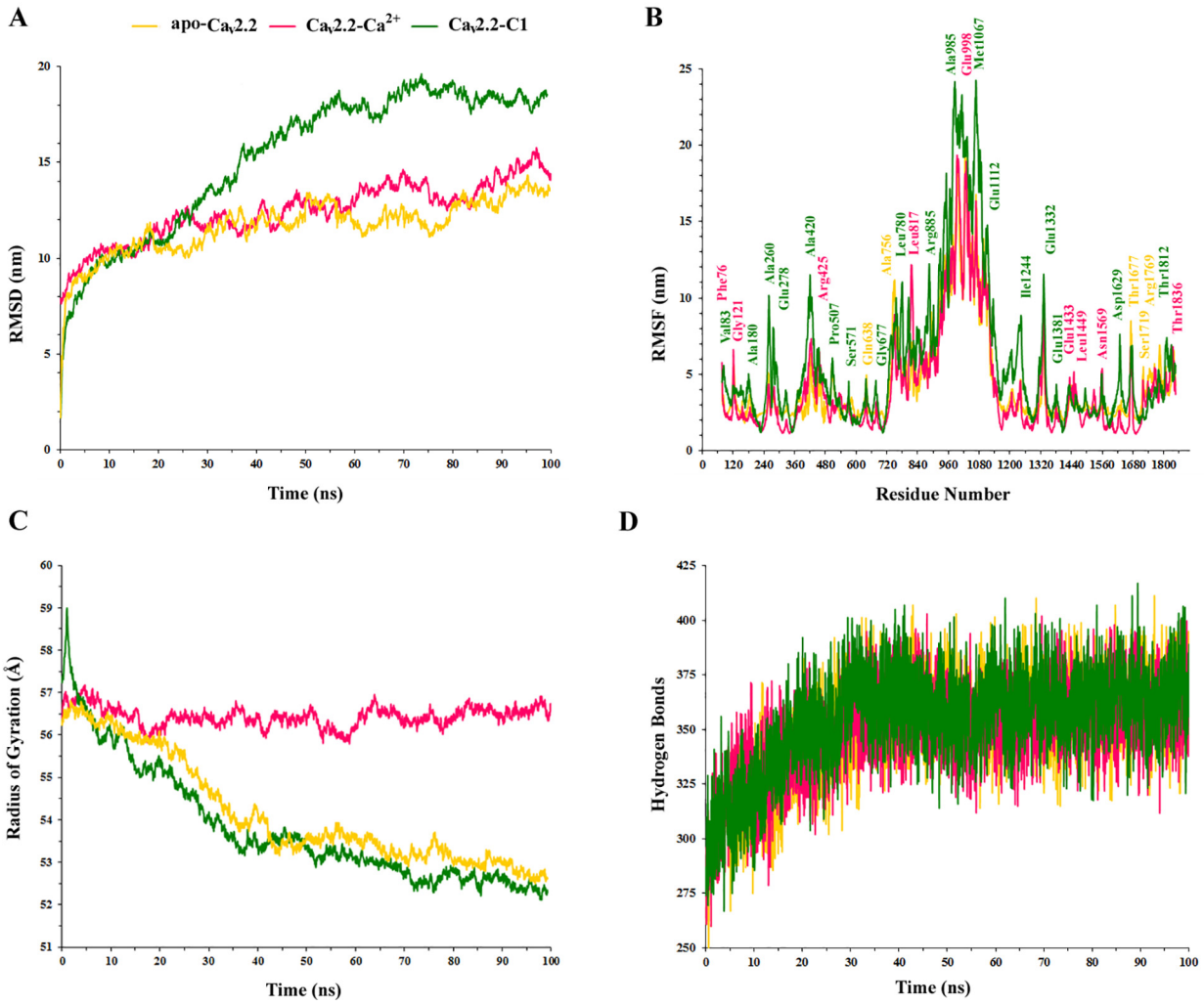

Fig. 5. Time-dependent analysis of apo-$Ca_v2.2$ (yellow), $Ca_v2.2$-Ca^{2+} ion (pink) and $Ca_v2.2$-C1 (green) complex at 100 ns. (A) RMSD versus time plot. (B) RMSF plot with labeled momentous fluctuating residues in respective colors. (C) Radius of gyration (Rg) plot with respect to time. (D) Hydrogen bonds analysis. (For interpretation of the references to color in this figure legend, the reader is referred to the web version of this article.)

Table 1
Root Mean Square Fluctuation (RMSF) for apo- $Ca_v2.2$, $Ca_v2.2$-Ca^{2+} ion and $Ca_v2.2$-C1 complex during 100 ns MD simulation.

Residues		Apo-$Ca_v2.2$ (nm)	$Ca_v2.2$-Ca^{2+} ion (nm)	$Ca_v2.2$-C1 (nm)
Selectivity filter (SF) ring	Glu314	2.39	1.18	2.24
	Glu663	2.26	1.35	2.14
	Glu1365	2.27	1.22	2.06
	Glu1655	2.26	1.12	2.69
G/A/A/A ring	Gly353	2.42	1.57	1.28
	Ala706	2.24	1.59	1.22
	Ala1413	2.06	1.60	1.76
	Ala1705	2.22	1.48	2.22
S4-S5 linker residues	Pro222	2.36	1.84	1.51
	Leu223	2.41	1.68	1.31
	Ser608	2.50	1.92	1.83
	Ile609	2.28	1.76	1.80
	Asn1281	2.13	1.50	2.07
	Val1282	2.09	1.50	2.07
	Lys1297	2.42	1.82	2.44
	Ala1598	2.46	2.13	2.41

Furthermore, g(r) plot results for Ca^{2+} ion and OE1 atoms of 4 glutamate residues (Glu314, Glu663, Glu1365 and Glu1655) were validated by distance calculation analysis through UCSF Chimera 1.11.2 for the PDB files generated at 10 ns and 99 ns of simulation time. Evidently, distances for Glu314, Glu663 and Glu1365 residues to Ca^{2+} ion were slightly reduced, while Glu1655 residue moved away (4.86 Å to 6.04 Å) from Ca^{2+} ion, indicating the movement of Ca^{2+} ion towards Glu314, Glu663 and Glu1365 residues (Fig. 6C,D).

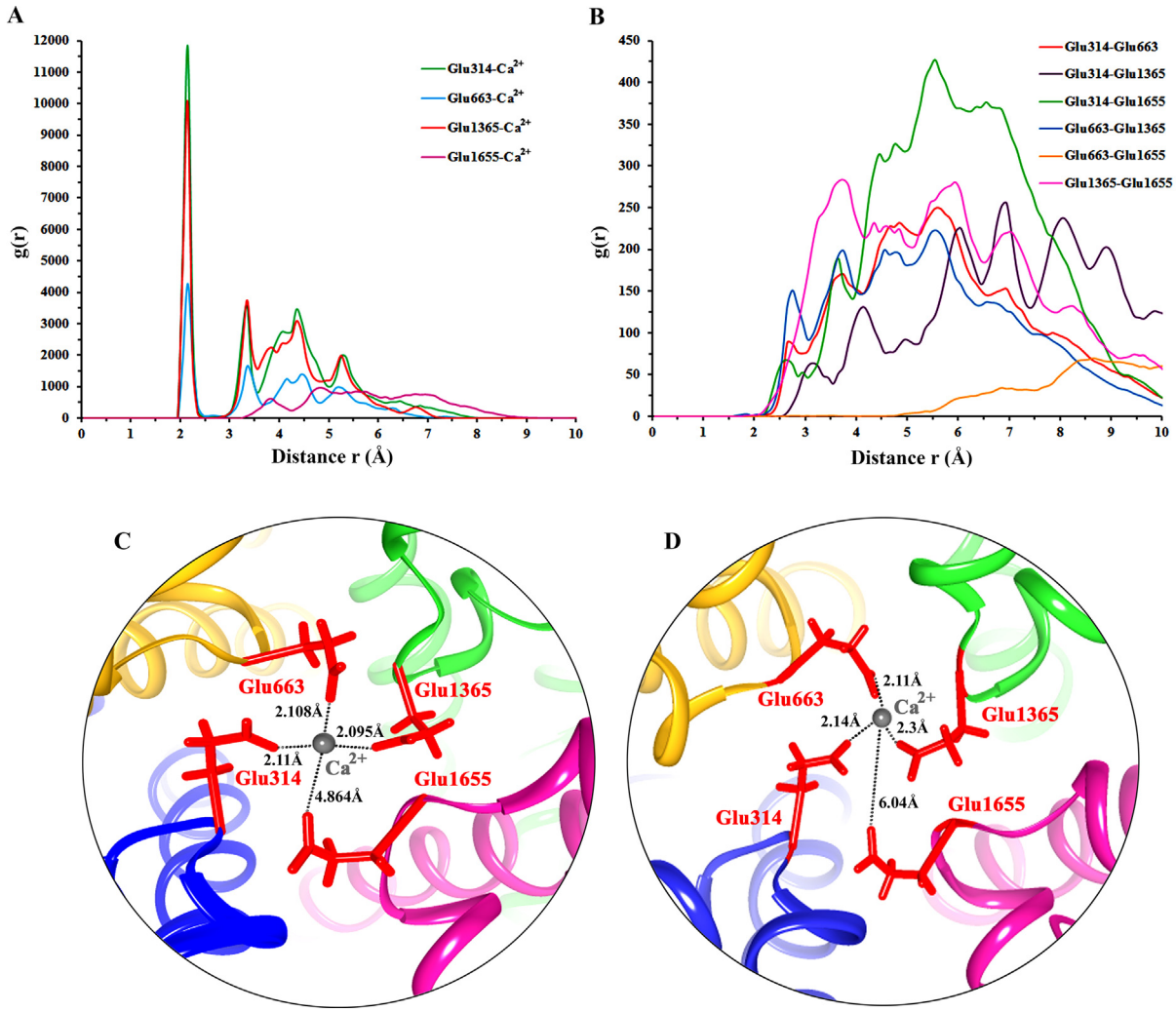

Fig. 6. Radial pair distribution function g(r) analysis. (A) g(r) plot for oxygen atoms (OE1) of 4 glutamate residues (Glu314, Glu663, Glu1365 and Glu1655) and Ca^{2+} ion. (B) g (r) plot for interatomic distances (OE1 atoms) of Glu314, Glu663, Glu1365 and Glu1655 residues. (C) and (D) Time-dependent distances measured by UCSF Chimera 1.11.2 among OE1 atoms of Glu314, Glu663, Glu1365 and Glu1655 residues and Ca^{2+} ion using PDB files generated at 10 ns and 99 ns of MD simulation run, respectively.

Table 2
Radial pair distribution function g(r) for Ca^{2+} ion and its selectivity filter (SF) ring residues in $Ca_v2.2$-Ca^{2+} ion complex.

Interaction between Glu- Ca^{2+} ion and Glu-Glu	Distances (Å)	Radial pair distribution function g(r)
Glu314 (OE1)-Ca^{2+} ion	2.15	11832.6
Glu663 (OE1)-Ca^{2+} ion	2.25	1837.5
Glu1365 (OE1)-Ca^{2+} ion	2.15	10041.5
Glu1655 (OE1)-Ca^{2+} ion	4.85	969.6
Glu314-Glu1365	6.95	255.4
Glu314-Glu1655	5.55	427.14
Glu314-Glu663	5.55	249.2
Glu663-Glu1365	5.55	223
Glu663-Glu1655	8.65	69.7
Glu1365-Glu1655	3.75	283.4

3.5. Conformational change analysis

Through comparative MD simulation analysis for $Ca_v2.2$-Ca^{2+} ion and $Ca_v2.2$-C1 complexes in comparison to apo-$Ca_v2.2$, details of critical residues including gating charge residues of VSDs, ion and inhibitor interacting residues at the pore region, pore lining residues, hydrophobic residues in the inner gate, S4-S5 linker interacting residues to S6 segments of pore domain were observed. Moreover, the influence of these residues in the opening and closing of $Ca_v2.2$ inner gate was explored in both systems, in particularly at SF and ion permeable regions of $Ca_v2.2$.

For $Ca_v2.2$-Ca^{2+} ion complex, all 4 domains (D_I-D_{IV}) were superimposed at 99 ns time scale (Fig. 7A). Though multiple structural variations were observed in all 4 domains (D_I-D_{IV}) of $Ca_v2.2$, divergence was more prominent at the loop and linker regions that allow the movement of individual segments during voltage sensing and inner gate opening/closing. These structural variations exhibited by D_I-D_{IV} domains may lead to asymmetric tetrameric conformation of $Ca_v2.2$. In this conformation, S1-S4 VSDs of $Ca_v2.2$ bear similar but non-identical structural features. Each $Ca_v2.2$ VSD contains four transmembrane α-helices (S1-S4). Upon superimposition, these transmembrane segments (S1-S4 VSDs) revealed an RMSD value of ~1.3 Å (Fig. 7A). Positively charged residues (Arg and Lys) of S4 segments at every third and fourth position were labeled as R1-R6. The human $Ca_v2.2$ S4 segment exhibits R1-R5 on VSD_I, R2-R6 on VSD_{II}, R1-R6 on VSD_{III} and R2-R6 residues on VSD_{IV} (Fig. 7A). In each VSD, S4 segment-specific gating charged residues were aligned at one side (Fig. 7B). R1-R4 residues were positioned above the conserved occluding Phe residue in CTC (charge transfer center), while R5 and R6 resides were lined below (Fig. 7C). Extracellular pointing of 4 out of 6 conserved R residues allow forming a depolarized or upstate generation. The upstate

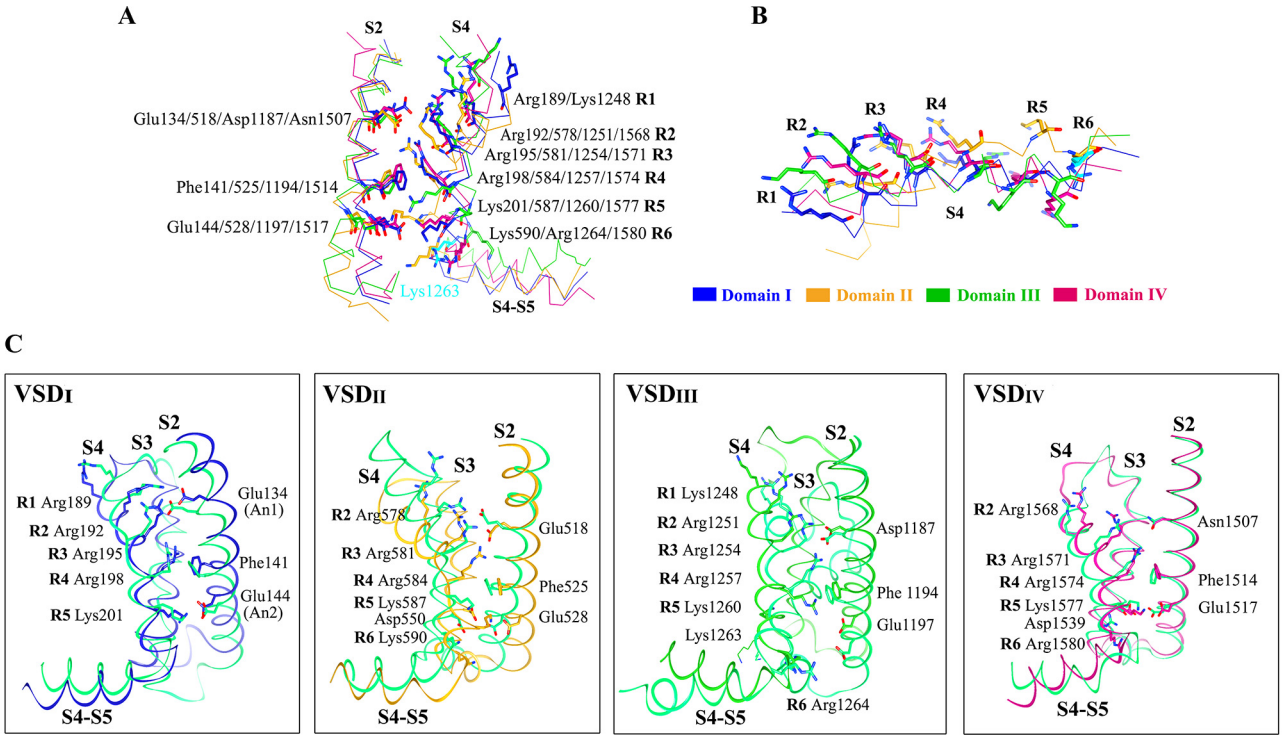

Fig. 7. Superimposition of four protomers. (A) Comparison of $VSD_{I\text{-}IV}$ S2 and S4 segments in $Ca_v2.2$-Ca^{2+} ion complex. Individual VSDs of $Ca_v2.2$ are colored blue, golden, lime green and violet red colors, respectively. The gating charge residues (R1-R6) in S4 and the shifted residue in S4 segment of VSD_{III} (cyan color) along with anion1 (An1), anion2 (An2) and occluding Phe residue in CTC (Charge Transfer Center) localized on S2 segment are shown as sticks, while S2 and S4 segments are indicated in wire form. The S2 and S4 segments of 4 VSDs are quite similar; however, they have high conformational divergence. (B) Side view of S4 segments. All the gating charge residues on S4 segments are aligned at one side of helix. (C-F) S2-S4 segments of 4 VSDs of $Ca_v2.2$-Ca^{2+} ion complex are structurally aligned relative to VSDs of $Ca_v2.2$-C1 complex. VSDs of Ca^{2+} ion-bound $Ca_v2.2$ are colored blue, golden, green and violet red colors, respectively. The inhibitor-bound $Ca_v2.2$ is shown in spring green color. (For interpretation of the references to color in this figure legend, the reader is referred to the web version of this article.)

levels may vary among different structures or within the domains of same structure. These levels are determined by gating charges due to residues above the bulky hydrophobic residue (Phe) of CTC [63]. The CTC is composed of conserved negative or polar residues including a highly conserved occluding bulky hydrophobic residue localized on S2 segment plus an invariant Asp residue, localized on S3 segment. These residues along with another polar or negatively charged residue (An1 and An2) of S2 segment contribute in the transmembrane movement by interacting with gating charged residues on S4 segment. In VSD tetramer, Glu134/518 residue localized on S2 of $VSD_{I,\ II}$, Asp1187 of VSD_{III} and Asn1507 of VSD_{IV} interact with R2 and R3, while R5 interacts with Glu144/528/1197/1517 of S2 segment. As evident in rabbit $Ca_v1.1$ [60], in human $Ca_v2.2$, Asp residues of VSD_{II} and VSD_{IV} S3 segments were observed in the formation of CTC (Fig. 7).

To observe structural conformations, VSDs were superimposed for both complexes ($Ca_v2.2$-Ca^{2+} ion and $Ca_v2.2$-C1). These results elucidated noticeable structural divergence where VSD_{II} and VSD_{III} exhibited prominent conformational changes at S3 and S4 segments (Fig. 7D, E). Remarkably, S4 and S3 helices of $Ca_v2.2$-Ca^{2+} ion and $Ca_v2.2$-C1 complexes displayed predominant kinks (Fig. 7-C-F). In contrast, $S2_{IV}$ and $S3_{IV}$ segments exhibited better structural alignment compared to other VSDs. Major conformational variations were observed in the S4-S5 linker region, revealing that during voltage sensing, the flexibility of linker region may have an influential role in the S4 segment movement.

3.6. Outer vestibule of $Ca_v2.2$

The primary structures of outer vestibule of all four domains of $Ca_v2.2$ exhibited well aligned SF residues (Fig. 8A). The simulated structures of both Ca^{2+} ion and C1-bound $Ca_v2.2$ revealed two rings of charged residues at the outer vestibule. The inner ring is composed of four negatively charge residues ($Glu314_I$, $Glu663_{II}$, $Glu1365_{III}$ and $Glu1655_{IV}$; the EEEE motif) neighbored by $Asp664_{II}$ and $Arg1650_{IV}$ [64]. The outer ring is composed of $Asp325_I$, $Arg1634_{IV}$ and $Glu1651_{IV}$. The hydrophobic ring was composed of $Ile319_I$, $Val668_{II}$, $Val1370_{III}$ and $Ile1660_{IV}$ residues that parted the outer and inner rings (Fig. 8B-C). Recent studies showed that ω-conotoxin GVIA forms salt bridges with the outer ring of $Ca_v2.2$; however, the apolar residues of hydrophobic ring sterically hinder the binding of toxin with the outer ring [64]. In our study, Ca^{2+}-bound $Ca_v2.2$ exhibited a wide groove at the pore region sourrounded by negatively charged residues that may allow Ca^{2+} ion binding at inner ring. Similarly, compound C1 interaction was mediated by SF ring in the pore. Such conformation may allow the appropriate binding of C1 with the pore residues of $Ca_v2.2$.

3.7. Analysis of $Ca_v2.2$ pore domain region

VSDs and pore structure are coupled in such a manner that S4 segment of VSD is connected to S5 of the pore domain via S4-S5 linker. Subsequently, a helical structure surrounds the pore domain and runs parallel to the intracellular side of membrane. Each VSD is localized adjacent to the neighboring pore domain and influences the gate of its own domain as well as of neighboring domain. Channel pore region and VSDs are coupled together due to direct interactions of S4-S5 linkers and S6 segments via Gly353 ($S6_I$), Ala706 ($S6_{II}$), Ala1413 ($S6_{III}$) and Ala1705 ($S6_{IV}$). Sequence alignment (Figs. S3, S4) and structural comparison of $Ca_v1.1$ and $Ca_v1.2$ channels indicate that instead of Gly residue in the $S6_{III}$ segments of $Ca_v1.1$ and $Ca_v1.2$ (G/A/G/A ring), $Ca_v2.2$ contains Ala residue that

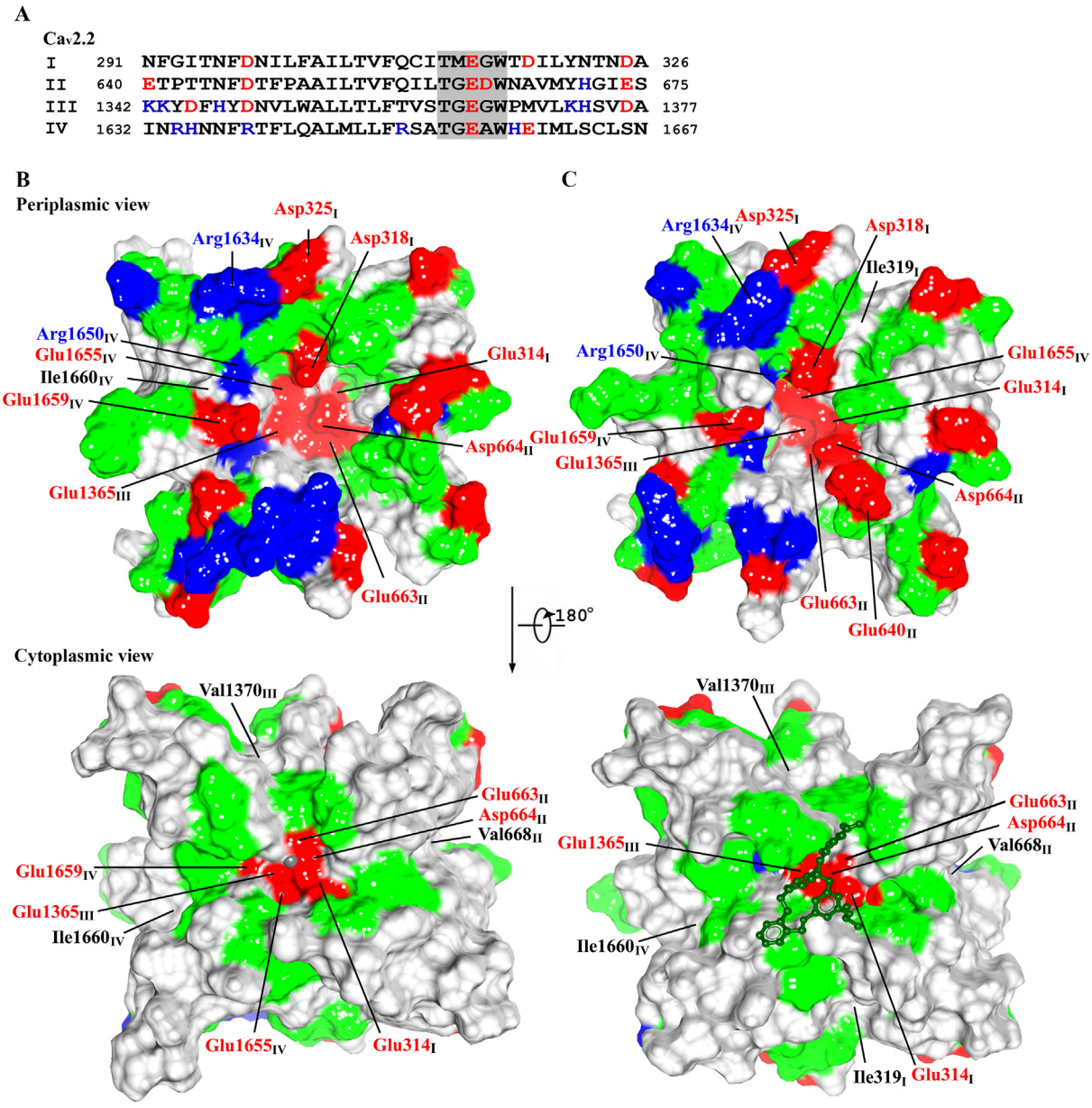

Fig. 8. Outer vestibule of four domains of $Ca_v2.2$. (A) Sequence alignment of $Ca_v2.2$ outer vestibule region in all four domains. The highlighted region signifies the selectivity filter lining residues. (B) Extracellular and cytosolic views of $Ca_v2.2$-Ca^{2+} ion complex outer vestibule. (C) Extracellular and cytosolic views of $Ca_v2.2$-C1 complex outer vestibule. Coloring scheme for residues are: hydrophobic, gray; polar, green; negatively charge, red and positively charge, blue. (For interpretation of the references to color in this figure legend, the reader is referred to the web version of this article.)

makes 'G/A/A/A ring' [65]. Recent studies potentiate that mutations of G/A/G/A residues impact the movement of VSDs [66]. The G/A/A/A position in the S6 is faced toward the S4-S5 linker to induce a direct interaction between them for tight packing. In apo-$Ca_v2.2$, the G/A/A/A ring residues lacked close interactions with loop residues localized between the S4-S5 linker and the S5 segment (Fig. 9B). In Ca^{2+}-bound $Ca_v2.2$, Gly353, Ala706 and Ala1413 residues were involved in interaction with the neighboring residues of loop region to facilitate the opening of channel pore at the entry gate for Ca^{2+} ions (Fig. 9D). In contrast, in $Ca_v2.2$-C1 complex, Ala1705 with Lys1597 and Ala1598 residues of the similar loop were involved in channel activity (Fig. 9F). Due to lack of Gly353, Ala706 and Ala1413 involvements in interaction, this loop moved towards S6 segment that prevented its interaction with S4-S5 linker residues and narrowed the tunnel at the inner gate to close the passage for ion flow.

Lys218-Leu223 ($S4_I$-$S5_I$) and Val1814-His1844 (IQ domain) regions of apo-$Ca_v2.2$ and $Ca_v2.2$-Ca^{2+}ion complex attained loop conformations (Fig. S7), while in $Ca_v2.2$-C1 complex; these regions adopted helical conformations (Fig. S8). The helical break of $S4_{III}$ was involved in kinking or bending the segment. $S3_{III}$ was positioned in parallel with the membrane as compared to other VSDs. The position of S4-S5 linker was also varied in all VSDs. In all systems, loop regions exhibited more fluctuations, except SF region of channel pore. Similarly, more conformational readjustments were visible at the EF-hand and IQ domains in all systems. The IQ domain was more inclined to inner gate of channel in $Ca_v2.2$-Ca^{2+} ion complex.

The pore domain of $Ca_v2.2$ exhibits a pseudo-four-fold symmetry similar to rabbit $Ca_v1.1$ [60]. At sequence level, the extracellular pore loop in the pore domain adjacent to SF of all 4 domains exhibited clear differences. In all systems, a close comparison among

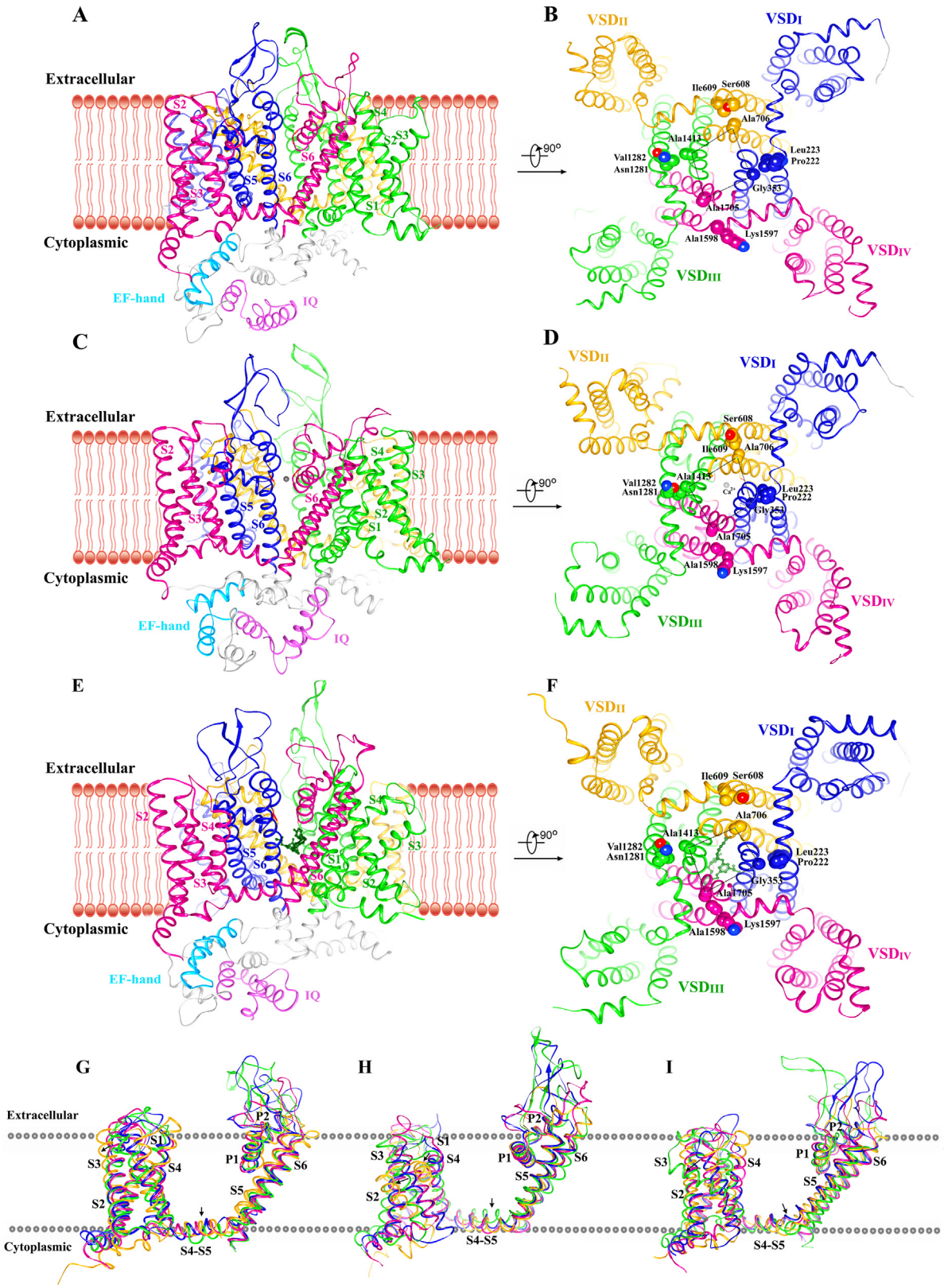

Fig. 9. Conformational transition analysis in apo-$Ca_v2.2$, $Ca_v2.2$ complex with Ca^{2+} ion and C1. (A), (C) and (E) Membrane topology and side views of apo-$Ca_v2.2$, $Ca_v2.2$-Ca^{2+} ion and $Ca_v2.2$-C1 complexes. D_I-D_{IV} domains are indicated in blue, gold, green and violet red colors, respectively. EF-hand domain is shown in sky blue, IQ domain is in orchid, Ca^{2+} ion in gray and C1 is indicated in dark green color. (B), (D) and (F) Cytosolic view of apo-$Ca_v2.2$, $Ca_v2.2$-Ca^{2+} ion and $Ca_v2.2$-C1 complexes. The dotted lines at the pore region indicate a cooperative unit. Residues of G/A/A/A ring on S6 and their interacting residues on S4-S5 linkers are labeled in black color. The spheres indicate their side chains. (G), (H) and (I) Side views of channel having superimposed 4 domains of apo-$Ca_v2.2$, $Ca_v2.2$-Ca^{2+} ion and $Ca_v2.2$-C1 complexes, respectively embedded in membrane at 67 ns time-scale. The domain segments are labeled in black color. (For interpretation of the references to color in this figure legend, the reader is referred to the web version of this article.)

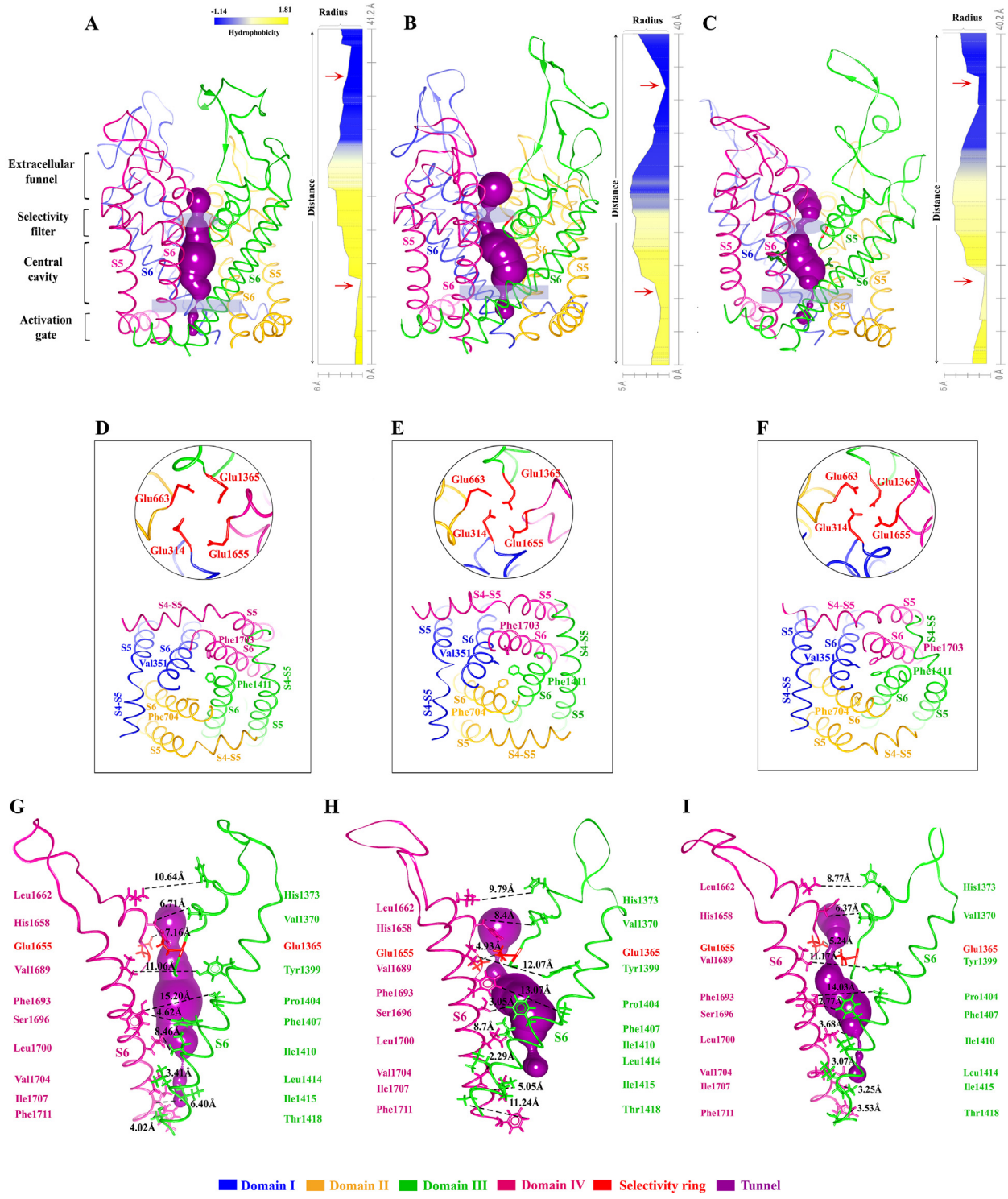

Fig. 10. Architecture and tunnel comparison in apo-$Ca_v2.2$, $Ca_v2.2$-Ca^{2+} and $Ca_v2.2$-C1 complexes. The VSDs have been omitted for better illustration. (A), (B) and (C) Side views of permeation path of pore domains for apo-$Ca_v2.2$, $Ca_v2.2$-Ca^{2+} ion and $Ca_v2.2$-C1structures, respectively. The ion conducting passage, calculated by MoleOnline (*https://mole.upol.cz/online/*) is illustrated by purple-colored tunnel. D_{I-IV} are indicated in blue, gold, green and violet red colors, respectively. Each segment of domain is labeled in the respective domain color. The Ca^{2+} ion is indicated in gray and C1 in dark green color. Pore radii along with the pore distances is displayed for each structure. Top red arrows indicate the ion selective and permeable regions localized at the narrowest tunnel (radius close to 0). Furthermore, the closest part of hydrophobic area (position close to 0) formed by Val351, Phe704, Phe1411 and Phe1703 residues is indicated by red arrows (bottom). The blue to yellow colored plot demonstrates the hydrophobic strength of pore forming residues. (D), (E) and (F) Circle displays extracellular view of SF residues of the pore region are indicated by red sticks for apo-$Ca_v2.2$, $Ca_v2.2$-Ca^{2+} ion and $Ca_v2.2$-C1 complexes, respectively. Cytoplasmic view of the occluding residues of inner gate (Val351, Phe704, Phe1411 and Phe1703) is shown in stick representation. (G), (H) and (I) Tunnel forming residues along with their distances measured by UCSF Chimera 1.11.2 for apo-$Ca_v2.2$, $Ca_v2.2$-Ca^{2+} and $Ca_v2.2$-C1 structures, respectively. Dotted lines indicate distances between adjacent residues of tunnel. Adjacent to tunnel, only two domains were shown to avoid ambiguity. (For interpretation of the references to color in this figure legend, the reader is referred to the web version of this article.)

repeats demonstrated that P-loop regions of D_I and D_{III} were longer than the P-loops of D_{II} and D_{IV} (Fig. 9). In addition, P-loops of D_I and D_{III} exhibited 1–2 pairs of antiparallel β-strands, respectively (Fig. 9). P-loop of D_{III} exhibited an extended conformation and more protrusion into the extracellular space. Through the P-loop region, α1 and α2 subunits were associated together. Upon superimposition of all 4 domains at 10, 60, 67 and 99 ns time scales, varying structural preferences were observed for individual VSD segments (Figs. S6, S7 and S8). Pronounced variations were visible in S3 and S4 segments (VSD_{II}) of apo-$Ca_v2.2$ and $Ca_v2.2$-Ca^{2+} ion complex, while in $Ca_v2.2$-C1 complex, VSD_{III} exhibited more bends within membrane (Fig. 9G-I, S6, S7 and S8). P1 and P2 helices of S3 and S4 segments were structurally similar in $Ca_v2.2$-Ca^{2+} ion complex than that of $Ca_v2.2$-C1 complex and apo-$Ca_v2.2$. S5 and S6 segments were conformationally dissimilar in both complexes. In case of $Ca_v2.2$-Ca^{2+} ion complex, S4-S5 linker helices of D_{III} were more divergent than others.

At the pore region, Glu residues (Glu314, Glu663, Glu1365 and Glu1655) localized at the periphery of ion selectivity region are clustered to regulate the tunnel passage (Fig. 10). The apo-$Ca_v2.2$ displayed a wide tunnel radius at SF region as compared to other two complexes (Fig. 10A-C). Underneath the selectivity filter vestibule, a typical hydrophobic cavity passes along with the side portals penetrated by transverse membrane lipids, a feature similar to rabbit $Ca_v1.1$ [45] and bacterial Na_v channels [67]. The asymmetric S6 bundle of $Ca_v2.2$ is tightly screwed at the inner activation gate. The apo-$Ca_v2.2$ and $Ca_v2.2$-C1 complex exhibited narrow tunnels in comparison to $Ca_v2.2$-Ca^{2+} ion complex, indicating a closed pore conformation through channel (Fig. 10A-C,G-I). Three aromatic residues (Phe704, Phe1411 and Phe1703), localized at the corresponding positions at $S6_{II-IV}$ along with Val351 of $S6_I$ (pore-occluding S6 residues) mediated the pore seal formation at the cytosolic region (Fig. 10D-F). Below the aromatic ring, hydrophobic residues of $S6_{I-II}$ (Leu and Gly/Ala) and $S6_{III-IV}$ (Val and Ala) facilitated in the channel closure. Furthermore, hydrophobic residues (Val351, Phe704, Phe1411 and Phe1703) lined at the narrowest point along the pore enclosed the entrance to the SF vestibule.

3.8. Structural comparison of human $Ca_v2.2$

In order to explore the open or close state of channel, $Ca_v2.2$-Ca^{2+} ion and $Ca_v2.2$-C1complexes were superimposed with apo-$Ca_v2.2$ simulated structure, relative to the pore domains. These structures revealed an RMSD value of ~1.24 Å (Fig. 11). The VSDs of apo-$Ca_v2.2$ possessed a depolarized or 'up' conformation and a closed inner gate, suggesting a potentially inactive state. All 4 homologous repeats/domains exhibit a counterclockwise arrangement when viewed from intracellular side and remain conserved in all eukaryotic calcium and sodium channels [60]. In our analysis, there was a subtle clockwise rotation of VSDs in Ca^{2+}-bound $Ca_v2.2$ VSD_{III} relative to apo-$Ca_v2.2$, while a counterclockwise rotation was observed in C1-bound $Ca_v2.2$ (Fig. 11). Moreover, a counterclockwise movement was detected in VSD_{II} of Ca^{2+}-bound $Ca_v2.2$ relative to apo-$Ca_v2.2$ (cytosolic view). The observations of inner gate suggested more distances among Cα atoms of $S6_{III}$ for Ca^{2+}-bound $Ca_v2.2$ in comparison to apo-$Ca_v2.2$ and C1-bound $Ca_v2.2$, whose inner gate is closed, while shorter distances were observed for $S6_I$, $S6_{II}$ and $S6_{IV}$ segments. Due to a kink in $S6_{IV}$ segment of C1 bound $Ca_v2.2$, apo-$Ca_v2.2$ exhibited more distance. Similarly, $S6_{II}$ segments of both apo and C1-bound $Ca_v2.2$ were

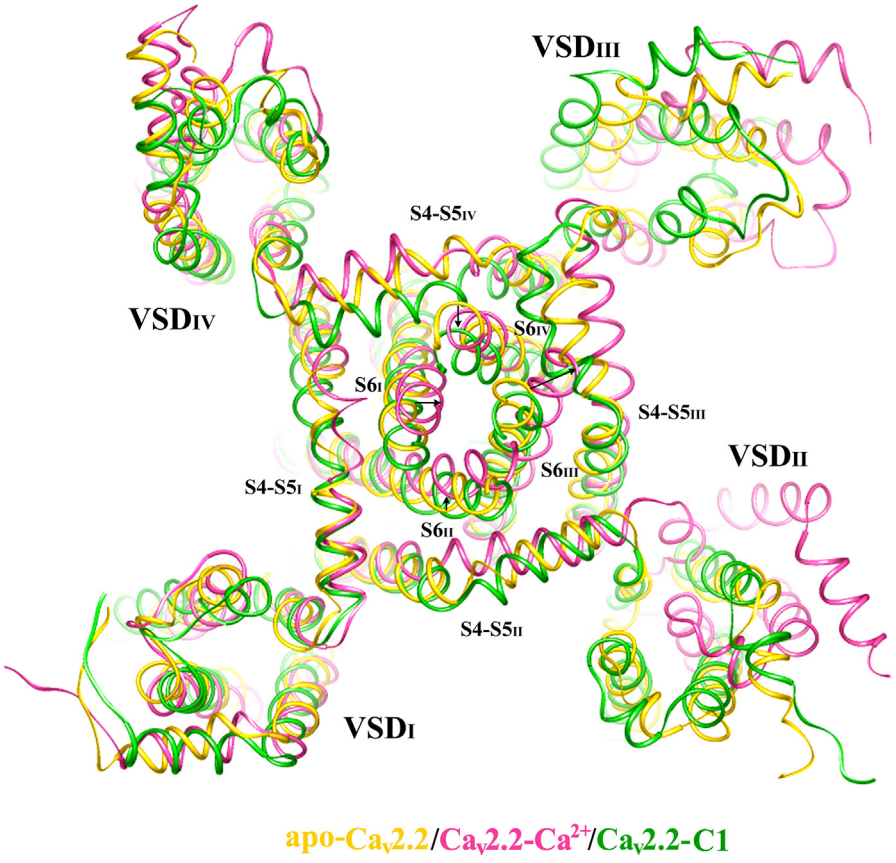

Fig. 11. Structural comparison of apo-$Ca_v2.2$with $Ca_v2.2$, Ca^{2+}- and C1-bound human $Ca_v2.2$. The pore domain superimposition demonstrates a clockwise rotation of VSDs in $Ca_v2.2$-Ca^{2+} ion complex (periplasmic view along the channel axis) relative to the apo-$Ca_v2.2$, with the exception of VSD_{II} that moves counterclockwise. Overall, C1-bound $Ca_v2.2$ reveals a subtle counterclockwise rotation.

different than that ofCav2.2 -Ca^{2+}- complex Overall, the inner gates of both apo-$Ca_v2.2$ and C1-bound $Ca_v2.2$ shared a similar conformational pattern. An inward movement of S6 segments in $Ca_v2.2$-C1 complex and a reduced pore size at the activation gate suggests that the gate is potentially closed. Thus the "up" (depolarized) conformation of VSDs and closed pore dimension may signify a potentially inactivated state of $Ca_v2.2$ upon C1 inhibitor binding.

4. Discussion

Chronic pain is considered as a major issue that affects the overall life quality of patient. Approximately, ~1.5 billion people are suffering with this condition globally [68]. Recently, a mouse model expressing N-type $Ca_v2.2$ VGCCs at the plasma membrane of peripheral somatosensory neurons via α2δ-1 accessory subunit revealed the role of these channels in pain modulation [69], suggesting that $Ca_v2.2$ Ca^{2+} channel may prove to be a potential drug target for novel analgesic therapies. Purposefully, the mimicry of venom peptides may hold a considerable promise due to lack of detailed structural information of neuronal ion channel. The non-peptide mimetics of MVIIA and GVIA ω-conotoxins isolated from marine cone snail efficiently bind to neuronal Ca^{2+} channels at low concentrations [9,62]. Here in this study, out of 30 known non-peptide analogues of ω-conotoxins (Table S1, Fig. S1), 7 peptides (Fig. 3; Table S2) were shortlisted on the basis of their binding abilities at the $Ca_v2.2$ pore region. These blockers bearing dendritic, benzothiazole or anthranilamide scaffolds (Fig. 3) may be used for the effective management of chronic and neuropathic pain by blocking $Ca_v2.2$ VGCCs.

Subsequently, through *in silico* analysis, we compared conformational ensemble of $Ca_v2.2$ bound to conopeptide-mimetic alkylphenyl ether-based analogue MVIIA (C1) [41] and Ca^{2+} ion to demonstrate potential anesthetic and analgesic impact of inhibitor. C1, initially proposed by Horwell group [70] contains a dendritic scaffold that mimics three key residues (Arg10, Leu11 and Tyr13) of MVIIA conotoxin [41]. In our analysis, the dendritic scaffold was found to be hydrophobically associated with Met313, Phe346 and Met347 residues of $Ca_v2.2$, while Glu1365 and Thr1363 residues were linked to Arg10 and Tyr13 of C1 via hydrogen bonding. In $Ca_v2.2$-C1 complex, RMSF profile comparison indicated significant transitions in Ala260, Ala420, D_{II}-D_{III} liker region (Ala985-Met1067, except Glu998 residue that exhibited more fluctuation in the Ca^{2+}-bound $Ca_v2.2$) and Glu1332 residue of C1-bound $Ca_v2.2$. Interestingly, upon Ca^{2+} ion permeability, D_{II}-D_{III} linker region acquired more stability than that of C1-bound $Ca_v2.2$. This linker region has been suggested as an important docking site for the binding of synaptic proteins [71]. The inhibitor-bound channel (52 Å) structure was more compact than Ca^{2+}-bound $Ca_v2.2$ (57 Å) indicating that Ca^{2+}-dependent structural destabilizing effects may lead in the channel opening (Fig. 5C). Possibly, Ca^{2+} ion-dependent opening of voltage-gated channel may create a functional binding site for synaptic vesicles in the N-type channels as reported in the recent studies [72,73]. Another evidence suggests that channel lacking D_{II}-D_{III} linker region is dramatically less sensitive to MVIIA and GVIA conotoxins than the full-length construct [74]. The presence of more structural rearrangements in the D_{II}-D_{III} linker region of C1-bound $Ca_v2.2$ may perhaps facilitate key residues for toxin binding. Our simulations delineate significant conformational changes at the proximal carboxyl-terminus (EF-hand and IQ domain helix) of $Ca_v2.2$ that attains an upright orientation upon Ca^{+2} ion permeability, (Fig. S7; Movie S2). In contrast, movement of C1-bound $Ca_v2.2$ IQ domain helix was totally different (Fig. S8; Movie S3). Possibly, such movements may be linked with the extent of channel opening at the activation gate. At IQ domain, a competitive binding of calmodulin (CaM) and Ca^{+2} binding proteins (CaBPs) influences the Ca^{+2}-dependent facilitation and inactivation of the Voltage-gated channels [75–78], while EF-hand motifs serve as Ca^{+2} ion sensors. Indeed, following the ion selectivity by Glu residues, such oscillations in the IQ helix and EF-hand orientation may provide a docking site for CaM association to induce auto-inhibitory mechanism by Ca^{+2} binding [79].

Evidently, SF ring is localized at the TM pore region with a large external vestibule or central cavity lined by the S6 segments and the intracellular activation gate formed due to intersection of S6 helices that exhibited more variations. Though tunnel lengths were quite comparable (41.2 Å, 40 Å and 40.2 Å, respectively), in contrast to apo-$Ca_v2.2$, both complexes ($Ca_v2.2$-Ca^{2+} and $Ca_v2.2$-C1) displayed remarkable changes in the architecture of channel tunnels (Fig. 10; Movie S4, S5). These findings illustrate that C1 binding to $Ca_v2.2$ induces more narrowing of the pore size at the activation gate as compared to Ca^{2+}-bound $Ca_v2.2$ due to differences in the hydrophilicity pattern at the selectivity region (Fig. 10F and 10G). Generally, the inner lining of tetrameric channel pore remains in the hydrophilic environment to allow the ion passage through the hydrophobic gate [80]. Subsequent occluding residues (Val351, Phe704, Phe1411 and Phe1703) facing the intracellular side contribute in the enhancement of hydrophobicity. Such dynamic structural rearrangements within the selectivity filter are crucial for channel gating [81]. In our analysis, a pronounced reduction in the tunnel volume at the selectivity filter and its enhancement at the activation gate of Ca^{+2}-bound $Ca_v2.2$ suggests that ion binding allows an outward splaying of pore-lining S6 helices to open the voltage gate. Recent evidence supports the movement of S6 helices in both sodium and potassium channels that is initiated at the hinge-point in the middle of the helix [82].

Collectively, given the analgesic efficacy and minimal side effects of ω-conotoxins [40], our study reveals MVIIA-associated structural implications and subtle changes in the $Ca_v2.2$ for the development of better therapeutic intervention for chronic and neuropathic pain. Clearly, MD-based conformational analysis of pain blocking ω-conotoxins may largely help in the potent inhibition of human presynaptic ion channels for devising promising therapeutic strategy.

CRediT authorship contribution statement

Sameera: Formal analysis, Investigation, Writing - original draft. **Fawad Ali Shah:** Formal analysis, Visualization. **Sajid Rashid:** Conceptualization, Project administration, Resources, Supervision, Validation, Writing - review & editing.

Acknowledgments

We acknowledge all members of Functional Informatics Lab, National Centre for Bioinformatics especially Saima Younis and Maryam Rozi for their indispensable help, support and encouragement.

Funding

This research did not receive any specific grant from funding agencies in the public, commercial, or not-for-profit sectors.

Declarations of interest

None.

Appendix A. Supplementary data

Supplementary data to this article can be found online at https://doi.org/10.1016/j.csbj.2020.08.027.

References

[1] Torrance N, Ferguson JA, Afolabi E, Bennett MI, Serpell MG, et al. Neuropathic pain in the community: more under-treated than refractory?. PAIN® 2013;154 (5):690–9.
[2] Mogil JS. Sex differences in pain and pain inhibition: multiple explanations of a controversial phenomenon. Nat Rev Neurosci 2012;13(12):859–66.
[3] Scholz J, Woolf CJ. Can we conquer pain?. Nat Neurosci 2002;5(11):1062–7.
[4] Jensen TS, Gottrup H, Sindrup SH, Bach FW. The clinical picture of neuropathic pain. Eur J Pharmacol 2001;429:1–3.
[5] Woolf CJ, Salter MW. Neuronal plasticity: increasing the gain in pain. Science 2000;288(5472):1765–8.
[6] Millan MJ. The induction of pain: an integrative review. Prog Neurobiol 1999;57(1):1–64.
[7] Attal N, Cruccu G, Haanpää M, Hansson P, Jensen TS, et al. EFNS guidelines on pharmacological treatment of neuropathic pain. Eur J Neurol 2006;13 (11):1153–69.
[8] Lee S. Pharmacological inhibition of voltage-gated Ca^{2+} channels for chronic pain relief. Curr Neuropharmacol 2013;11(6):606–20.
[9] Schroeder CI, Lewis RJ. ω-conotoxins GVIA, MVIIA and CVID: SAR and clinical potential. Mar Drugs 2006;4(3):193–214.
[10] Williams JA, Day M, Heavner JE. Ziconotide: an update and review. Expert Opin Pharmacother 2008;9(9):1575–83.
[11] McGivern JG. Ziconotide: a review of its pharmacology and use in the treatment of pain. Neuropsychiatr Dis Treat 2007;3(1):69.
[12] Bear B, Asgian J, Termin A, Zimmermann N. Small molecules targeting sodium and calcium channels for neuropathic pain. Curr Opin Drug Discov Devel 2009;12(4):543–61.
[13] Yamamoto T, Takahara A. Recent updates of N-type calcium channel blockers with therapeutic potential for neuropathic pain and stroke. Curr Top Med Chem 2009;9(4):377–95.
[14] Cizkova D, Marsala J, Lukacova N, Marsala M, Jergova S, et al. Localization of N-type Ca 2+ channels in the rat spinal cord following chronic constrictive nerve injury. Exp Brain Res 2002 Dec 1;147(4):456–63.
[15] Yokoyama K, Kurihara T, Makita K, Tanabe T. Plastic change of N-type Ca channel expression after preconditioning is responsible for prostaglandin E2-induced long-lasting allodynia. Anesthesiology 2003;99(6):1364–70.
[16] Hatakeyama S, Wakamori M, Ino M, Miyamoto N, Takahashi E, et al. Differential nociceptive responses in mice lacking the α1B subunit of N-type Ca^{2+} channels. NeuroReport 2001;12(11):2423–7.
[17] Kim C, Jun K, Lee T, Kim SS, McEnery MW, et al. Altered nociceptive response in mice deficient in the α1B subunit of the voltage-dependent calcium channel. Mol Cell Neurosci 2001;18(2):235–45.
[18] Saegusa H, Kurihara T, Zong S, Kazuno AA, Matsuda Y, et al. Suppression of inflammatory and neuropathic pain symptoms in mice lacking the N-type Ca^{2+} channel. EMBO J 2001;20(10):2349–56.
[19] Yaksh TL. Calcium channels as therapeutic targets in neuropathic pain. The Journal of Pain. 2006;7(1):S13–30.
[20] Altier C, Zamponi GW. Targeting Ca^{2+} channels to treat pain: T-type versus N-type. Trends Pharmacol Sci 2004;25(9):465–70.
[21] Sabido-David C, Faravelli L, Salvati P. The therapeutic potential of Na^{+} and Ca^{2+} channel blockers in pain management. Expert Opin Invest Drugs 2004;13 (10):1249–61.
[22] Winquist RJ, Pan JQ, Gribkoff VK. Use-dependent blockade of $Ca_v2.2$ voltage-gated calcium channels for neuropathic pain. Biochem Pharmacol 2005;70 (4):489–99.
[23] Wadel K, Neher E, Sakaba T. The coupling between synaptic vesicles and Ca^{2+} channels determines fast neurotransmitter release. Neuron 2007;53(4):563–75.
[24] Wheeler DG, Groth RD, Ma H, Barrett CF, Owen SF, et al. $Ca(V)_1$ and $Ca(V)_2$ channels engage distinct modes of Ca(2+) signaling to control CREB-dependent gene expression. Cell 2012;149(5):1112–24.
[25] Stanika RI, Villanueva I, Kazanina G, Andrews SB, Pivovarova NB. Comparative impact of voltage-gated calcium channels and NMDA receptors on mitochondria-mediated neuronal injury. J Neurosci 2012;32(19):6642–50.
[26] Simms BA, Zamponi GW. Trafficking and stability of voltage-gated calcium channels. Cell Mol Life Sci 2012;69(6):843–56.
[27] Park J, Luo ZD. Calcium channel functions in pain processing. Channels. 2010;4 (6):510–7.
[28] Catterall WA. Structure and regulation of voltage-gated Ca^{2+} channels. Annu Rev Cell Dev Biol 2000;16(1):521–55.
[29] Hofmann F, Biel M, Flockerzi V. Molecular basis for Ca^{2+} channel diversity. Annu Rev Neurosci 1994;17(1):399–418.
[30] Flynn R, Zamponi G. Calcium channel regulation by RGK proteins. Channels. 2010 Nov;4(6):434–9.
[31] Hidalgo P, Neely A. Multiplicity of protein interactions and functions of the voltage-gated calcium channel β-subunit. Cell Calcium 2007;42(4–5):389–96.
[32] Karunasekara Y, Dulhunty AF, Casarotto MG. The voltage-gated calcium-channel β subunit: more than just an accessory. Eur Biophys J 2009 Dec 1;39 (1):75–81.
[33] Carstens BB, Clark JR, Daly LN, Harvey JP, Kaas Q, et al. Engineering of conotoxins for the treatment of pain. Curr Pharm Des 2011;17(38):4242–53.
[34] Fry BG, Roelants K, Champagne DE, Scheib H, Tyndall JD, et al. The toxicogenomic multiverse: convergent recruitment of proteins into animal venoms. Annu Rev Genomics Hum Genet 2009;22(10):483–511.
[35] Lewis RJ, Garcia ML. Therapeutic potential of venom peptides. Nat Rev Drug Discov 2003;2(10):790–802.
[36] Tedford HW, Sollod BL, Maggio F, King GF. Australian funnel-web spiders: master insecticide chemists. Toxicon 2004;43(5):601–18.
[37] Olivera BM. Conus snail venom peptides. In: Handbook of Biologically Active peptides. Academic Press; 2006. p. 381–8.
[38] Baell JB, Duggan PJ, Forsyth SA, Lewis RJ, Lok YP, et al. Synthesis and biological evaluation of nonpeptide mimetics of ω-conotoxin GVIA. Bioorg Med Chem 2004;12(15):4025–37.
[39] Nielsen KJ, Schroeder T, Lewis R. Structure–activity relationships of ω-conotoxins at N-type voltage-sensitive calcium channels. J Mol Recognit 2000;13(2):55–70.
[40] Tranberg CE, Yang A, Vetter I, McArthur JR, Baell JB, et al. ω-Conotoxin GVIA mimetics that bind and inhibit neuronal Cav2. 2 ion channels. Mar Drugs 2012 Oct;10(10):2349–68.
[41] Menzler S, Bikker JA, Suman-Chauhan N, Horwell DC. Design and biological evaluation of non-peptide analogues of omega-conotoxin MVIIA. Bioorg Med Chem Lett 2000;10(4):345–7.
[42] Baell JB, Duggan PJ, Lok YP. ω-Conotoxins and approaches to their non-peptide mimetics. Aust J Chem 2004;57(3):179–85.
[43] Baell JB, Duggan PJ, Forsyth SA, Lewis RJ, Lok YP, et al. Synthesis and biological evaluation of anthranilamide-based non-peptide mimetics of ω-conotoxin GVIA. Tetrahedron 2006;62(31):7284–92.
[44] Andersson A, Baell JB, Duggan PJ, Graham JE, Lewis RJ, et al. ω-Conotoxin GVIA mimetics based on an anthranilamide core: Effect of variation in ammonium side chain lengths and incorporation of fluorine. Bioorg Med Chem 2009;17 (18):6659–70.
[45] Wu J, Yan Z, Li Z, Qian X, Lu S, et al. Structure of the voltage-gated calcium channel Ca v 1.1 at 3.6 Å resolution. Nature 2016;537(7619):191–6.
[46] Pettersen EF, Goddard TD, Huang CC, Couch GS, Greenblatt DM, et al. UCSF Chimera—a visualization system for exploratory research and analysis. J Comput Chem 2004;25(13):1605–12.
[47] Emsley P, Lohkamp B, Scott WG, Cowtan K. Features and development of Coot. Acta Crystallogr D Biol Crystallogr 2010;66(4):486–501.
[48] Duggan PJ, Lewis RJ, Lok YP, Lumsden NG, Tuck KL, et al. Low molecular weight non-peptide mimics of ω-conotoxin GVIA. Bioorg Med Chem Lett 2009;19 (10):2763–5.
[49] Mills N. ChemDraw Ultra 10.0 CambridgeSoft, 100 CambridgePark Drive, Cambridge, MA 02140. www.cambridgesoft.com.
[50] Hanwell MD, Curtis DE, Lonie DC, Vandermeersch T, Zurek E, et al. Avogadro: an advanced semantic chemical editor, visualization, and analysis platform. J Cheminf 2012;4(1):17.
[51] Halgren TA. Merck molecular force field. I. Basis, form, scope, parameterization, and performance of MMFF94. J Comput Chem 1996;17(5–6):490–519.
[52] Schneidman-Duhovny D, Inbar Y, Nussinov R, Wolfson HJ. PatchDock and SymmDock: servers for rigid and symmetric docking. Nucleic Acids Res 2005;33(suppl_2):W363–7.
[53] Wallace AC, Laskowski RA, Thornton JM. LIGPLOT: a program to generate schematic diagrams of protein-ligand interactions. Protein Eng Des Sel 1995;8 (2):127–34.
[54] BIOVIA DS. BIOVIA Discovery Studio 2017 R2: A comprehensive predictive science application for the Life Sciences. San Diego, CA, USA http://accelrys.com/products/collaborative-science/biovia-discovery-studio. 2017.
[55] Humphrey W, Dalke A, Schulten K. VMD: visual molecular dynamics. J Mol Graph 1996;14(1):33–8.
[56] Phillips JC, Braun R, Wang W, Gumbart J, Tajkhorshid E, et al. Scalable molecular dynamics with NAMD. J Comput Chem 2005;26(16):1781–802.
[57] Grubmüller H. SOLVATE v. 1.0. Theoretical Biophysics Group. Institute for Medical Optics, Ludwig-Maximilians University, Munich. 1996.
[58] MacKerell Jr AD, Bashford D, Bellott ML, Dunbrack Jr RL, Evanseck JD, et al. All-atom empirical potential for molecular modeling and dynamics studies of proteins. J Phys Chem B 1998;102(18):3586–616.
[59] Zoete V, Cuendet MA, Grosdidier A, Michielin O. SwissParam: a fast force field generation tool for small organic molecules. J Comput Chem 2011;32 (11):2359–68.
[60] Wu J, Yan Z, Li Z, Yan C, Lu S, et al. Structure of the voltage-gated calcium channel Cav1. 1 complex. Science. 2015 Dec 18;350(6267):aad2395.
[61] Finn BE, Evenäs J, Drakenberg T, Waltho JP, Thulin E, et al. Calcium-induced structural changes and domain autonomy in calmodulin. Nat Struct Biol 1995;2(9):777–83.
[62] Duggan PJ, Tuck KL. Bioactive mimetics of conotoxins and other venom peptides. Toxins. 2015;7(10):4175–98.
[63] Bezanilla F. The voltage sensor in voltage-dependent ion channels. Physiol Rev 2000;80(2):555–92.
[64] Chen R, Chung SH. Complex structures between the N-type calcium channel (CaV2.2) and ω-conotoxin GVIA predicted via molecular dynamics. Biochemistry 2013;52(21):3765–72.
[65] Hering S, Zangerl-Plessl EM, Beyl S, Hohaus A, Andranovits S, et al. Calcium channel gating. Pflügers Archiv-European Journal of Physiology. 2018;470 (9):1291–309.

[66] Beyl S, Depil K, Hohaus A, Stary-Weinzinger A, Linder T, et al. Neutralisation of a single voltage sensor affects gating determinants in all four pore-forming S6 segments of Ca V 1.2: a cooperative gating model. Pflügers Archiv-Eur J Physiol 2012;464(4):391–401.
[67] Zhang X, Ren W, DeCaen P, Yan C, Tao X, et al. Crystal structure of an orthologue of the NaChBac voltage-gated sodium channel. Nature 2012;486 (7401):130–4.
[68] Stevens EB, Stephens GJ. Recent advances in targeting ion channels to treat chronic pain. Br J Pharmacol 2018;175(12):2133.
[69] Nieto-Rostro M, Ramgoolam K, Pratt WS, Kulik A, Dolphin AC. Ablation of α2δ-1 inhibits cell-surface trafficking of endogenous N-type calcium channels in the pain pathway in vivo. Proc Natl Acad Sci 2018 Dec 18;115(51):E12043–52.
[70] Menzler S, Bikker JA, Horwell DC. Synthesis of a non-peptide analogue of omega-conotoxin MVIIA. Tetrahedron Lett 1998;39(41):7619–22.
[71] Sheng ZH, Rettig J, Takahashi M, Catterall WA. Identification of a syntaxin-binding site on N-type calcium channels. Neuron 1994;13(6):1303–13.
[72] Kiyonaka S, Wakamori M, Miki T, Uriu Y, Nonaka M, et al. RIM1 confers sustained activity and neurotransmitter vesicle anchoring to presynaptic Ca 2+ channels. Nat Neurosci 2007;10(6):691–701.
[73] Han Y, Kaeser PS, Südhof TC, Schneggenburger R. RIM determines Ca^{2+} channel density and vesicle docking at the presynaptic active zone. Neuron 2011;69 (2):304–16.
[74] Kaneko S, Cooper CB, Nishioka N, Yamasaki H, Suzuki A, et al. Identification and characterization of novel human Cav2. 2 (α1B) calcium channel variants lacking the synaptic protein interaction site. J Neurosci 2002;22(1):82–92.
[75] Qin N, Olcese R, Bransby M, Lin T, Birnbaumer L. Ca^{2+}-induced inhibition of the cardiac Ca^{2+} channel depends on calmodulin. Proc Natl Acad Sci 1999;96 (5):2435–8.
[76] Pitt GS, Zühlke RD, Hudmon A, Schulman H, Reuter H, et al. Molecular basis of calmodulin tethering and Ca^{2+}-dependent inactivation of L-type Ca^{2+} channels. J Biol Chem 2001;276(33):30794–802.
[77] Zhou H, Yu K, McCoy KL, Lee A. Molecular mechanism for divergent regulation of Cav1. 2 Ca^{2+} channels by calmodulin and Ca^{2+}-binding protein-1. J Biol Chem 2005;280(33):29612–9.
[78] Cui G, Meyer AC, Calin-Jageman I, Neef J, Haeseleer F, et al. Ca^{2+}-binding proteins tune Ca^{2+}-feedback to Cav1. 3 channels in mouse auditory hair cells. J Physiol 2007;585(3):791–803.
[79] Mori MX, Vander Kooi CW, Leahy DJ, Yue DT. Crystal structure of the CaV2 IQ domain in complex with Ca^{2+}/calmodulin: high-resolution mechanistic implications for channel regulation by Ca^{2+}. Structure 2008;16(4):607–20.
[80] Yonkunas M, Kurnikova M. The hydrophobic effect contributes to the closed state of a simplified ion channel through a conserved hydrophobic patch at the pore-helix crossing. Front Pharmacol 2015;27(6):284.
[81] McCoy JG, Nimigean CM. Structural correlates of selectivity and inactivation in potassium channels. Biochim Biophys Acta (BBA)-Biomembr 2012;1818(2):272–85.
[82] Domene C, Doyle DA, Vénien-Bryan C. Modeling of an ion channel in its open conformation. Biophys J 2005;89(1):L01–L3.
[83] Schroeder CI, Smythe ML, Lewis RJ. Development of small molecules that mimic the binding of ω-conotoxins at the N-type voltage-gated calcium channel. Mol Diversity 2004;8(2):127–34.
[84] Baell JB, Duggan PJ, Forsyth SA, Lewis RJ, Lok YP, Schroeder CI, et al. Synthesis and biological evaluation of anthranilamide-based non-peptide mimetics of ω-conotoxin GVIA. Tetrahedron 2006;62(31):7284–92.
[85] Gleeson EC, Graham JE, Spiller S, Vetter I, Lewis RJ, Duggan PJ, et al. Inhibition of N-type calcium channels by fluorophenoxyanilide derivatives. Mar Drugs 2015;13(4):2030–45.